

LOW TEMPERATURE FORMIC ACID DECOMPOSITION PATHWAYS ON
SUPPORTED PALLADIUM NANOPARTICLES

By

Sierra Schlusser

A thesis submitted to the Faculty and The Board of Trustees of the Colorado School of Mines in partial fulfillment of the requirements of the degree of Master of Science (Chemical and Biological Engineering).

Golden, Colorado

Date: _____

Signed: _____

Sierra Schlusser

Signed: _____

Dr. Stephanie Kwon

Thesis Advisor

Golden, Colorado

Date: _____

Signed: _____

Dr. Nanette Boyle

Professor and Head

Department of Chemical and Biological Engineering

ABSTRACT

Formic acid (HCOOH) has emerged as a promising liquid hydrogen (H₂) carrier due to its low toxicity, low flammability, and ease of handling. The utilization of HCOOH as a potential liquid H₂ carrier requires a catalytic system that selectively dehydrogenates HCOOH at low temperatures without forming any dehydration products (CO) that can act as a poison for Pt electrodes in fuel cell applications. Pd-based catalysts are widely studied for this reaction due to its high reactivity at low temperatures. Yet, details of the reaction pathways and intermediates of HCOOH dehydrogenation on Pd-based catalysts have remained inconclusive. The catalytic stability and selectivity of Pd nanoparticles have remained controversial in current literature.

This work combines kinetic, isotopic, and spectroscopic methods to investigate the viability, reaction mechanism, and particle size effects of Pd/SiO₂ catalysts for HCOOH decomposition pathways. In doing so, we show that supported Pd catalysts are highly active and selective towards the dehydrogenation products (H₂/CO₂) at low temperatures (≤ 383 K) without any detectable formation of dehydration products (H₂O/CO). No apparent deactivation was observed up to 60 ks time-on-stream. In-situ infrared spectra measured at a range of HCOOH pressures (0.17-3.36 kPa; 353 K) detected molecularly bound HCOOH (HCOOH*) as the reaction intermediate. Such results contradict the formation of carboxylates (COOH*) and/or formates (HCOO*) that have been proposed as reactive intermediates in literature. Additional kinetic studies showed that the reaction followed a first-order reaction at low HCOOH pressures, which transitioned into zeroth-order reaction at higher pressures. Isotopic studies with DCOOH and HCOOD show that both the cleaving of the O-H and C-H bonds are kinetically relevant steps. The change in Pd loading on the SiO₂ support showed the importance of particle size on the rate of reaction. The smaller the particles, the more reactive they are, allowing for higher turnover rates. The results from this study can be utilized to provide design strategies for Pd-based catalysts for their use in HCOOH dehydrogenation reactions for its potential use as a liquid H₂ carrier at industrial scale.

TABLE OF CONTENTS

ABSTRACT.....	iii
LIST OF FIGURES	vi
LIST OF TABLES	viii
LIST OF SCHEMES.....	ix
ACKNOWLEDGEMENTS	x
CHAPTER 1 INTRODUCTION	1
1.1. Importance of Hydrogen Storage Technology.....	1
1.2. Formic Acid as a Potential Liquid Hydrogen Carrier	2
1.3. Metal Based Catalysts for Formic Acid Dehydrogenation	4
1.4. Outline of Thesis.....	5
CHAPTER 2 BACKGROUND	7
2.1. Mechanism of Formic Acid Decomposition on Metal Surfaces	7
2.2. Formic Acid Decomposition Routes on Palladium Based Catalysts	8
CHAPTER 3 FORMIC ACID DECOMPOSITION PATHWAYS ON SUPPORTED PALLADIUM NANOPARTICLES AT NEAR AMBIENT TEMPERATURES	13
3.1. Introduction.....	13
3.3. Methods.....	15
3.3.1. Catalyst Preparation and Characterization.....	15
3.3.2. In-Situ Infrared Spectroscopy.....	16
3.3.3. Kinetic Analysis	17
3.3.4. Temperature Programmed Desorption (TPD)	18
3.4. Results and Discussion	18
3.4.1. Formic Acid Decomposition Rates, Selectivities, and Stabilities on Pd/SiO ₂	18
3.4.2. Reaction Kinetics	19
3.4.3. Pd Size Effects.....	33
3.5. Conclusion.....	34
3.6. Acknowledgements	35

CHAPTER 4 CONCLUSIONS AND FUTURE WORK.....	36
4.1. Conclusions.....	36
4.2. Future Work.....	37
REFERENCES	38
APPENDIX A COPYRIGHT PERMISSIONS.....	44

LIST OF FIGURES

Figure 1.1.	HCOOH hydrogenation-dehydrogenation pathway and desired products, based on reported data from Ref. ¹²	4
Figure 1.2.	Decomposition temperature ($T_r(K)$) of adsorbed formates on metallic powders from TPD measurements as a function of formate binding energies on metal (111) surfaces from DFT methods. (Reproduced with permission from Ref. ²⁶ , Copyright 2016, Elsevier).....	5
Figure 2.1.	Schematic of HCOOH decomposition pathways on transition metal surfaces, based on the proposed mechanisms discussed in Ref. ^{47,48} . (Reproduced with permission from Ref. ¹² , Copyright 2022, Springer Nature).....	8
Figure 2.2.	DFT-derived energy (eV) of reactive intermediates and transition states involved in HCOO* and COOH* pathways on Pd(100) (solid lines) and Pd(111) (dashed lines) surfaces. The arrows show the downshift in transition state energy on Pd(100) compared to Pd(111). (Reproduced with permission from Ref. ³⁶ , Copyright 2021, Elsevier).....	10
Figure 2.3.	Apparent activation energy of HCOOH dehydrogenation (1 M HCOOH in H ₂ O; 303-333 K) on Pd/C (left axis) and the decomposition temperature of PdH _x , measured from TPD analysis after reduction of Pd/C at 373 K in H ₂ (the right axis) as a function of average Pd sizes (from TEM images) (Reproduced with permission from Ref. ⁵⁰ , Copyright 2019, Elsevier).....	11
Figure 3.1.	HCOOH dehydrogenation turnover rate (per surface Pd atom) measured on Pd/SiO ₂ (1% wt.) as a function of time on stream (0.84 kPa HCOOH, 383 K). Dashed line represents the trend line.	20
Figure 3.2.	HCOOH dehydrogenation turnover rates (per surface Pd atom) measured on Pd/SiO ₂ (1% wt.) as a function of HCOOH pressure at a range of temperatures (0.17-3.36 kPa; 353-383 K). The dashed curves represent the optimal regression rates using the functional form of Eq. (3.1).....	21
Figure 3.3.	HCOOH dehydrogenation turnover rates (per surface Pd atom) measured with H ₂ co-feed on Pd/SiO ₂ (1% wt.) as a function of H ₂ pressure (0-33.6 kPa H ₂ , 0.25 and 2.52 kPa HCOOH; 363 K). Dashed lines represent the trend lines.....	22
Figure 3.4.	HCOOH dehydrogenation turnover rates (per surface Pd atom) measured on Pd/SiO ₂ (1% wt.) as a function of HCOOH pressure for varying aggregate sizes (0.17-3.36 kPa; 383 K). Dashed curves represent the optimal regression rates using the functional form of Eq. (3.1).....	23
Figure 3.5.	DFT-derived infrared spectra (PBE-D3) of HCOOH*, HCOO _M *, HCOO _B * and COOH* on Pd(111) surface (provided by Michelle Nolen).....	24

Figure 3.6.	(a) Infrared spectra of Pd/SiO ₂ (1% wt.) measured during steady-state HCOOH catalysis (0.17-3.36 kPa; 353 K). (b) 1000-1900 cm ⁻¹ section of spectra labelled with significant bands (HCOOH(g) (1790, 1747, 1364, 1211, 1118 and 1090 cm ⁻¹) and HCOOH* (1570 cm ⁻¹)).....	25
Figure 3.7.	Infrared spectra of Pd/SiO ₂ (1% wt.) measured during steady-state HCOOH catalysis (0.17-3.36 kPa; 353 K). Significant bands are labelled (CO ₂ (2360 cm ⁻¹ , 2340 cm ⁻¹)) and expected band area of CO (2180 cm ⁻¹ , 2100 cm ⁻¹) and CO* (2065 cm ⁻¹) are highlighted.....	26
Figure 3.8.	(a) Absorbance of HCOOH(g) and CO ₂ (g) on Pd/SiO ₂ (1% wt.) measured during steady-state HCOOH catalysis (0.17-3.36 kPa HCOOH, 353 K). The dashed lines represent the trend lines. (b) Surface coverage ratio of HCOOH* band on Pd/SiO ₂ (1% wt.) measured during steady-state HCOOH catalysis (0.17-3.36 kPa HCOOH, 353 K). Dashed curve represents the optimal regression of the rate using the functional form of Eq. (3.2).....	28
Figure 3.9.	a) Infrared spectra of Pd/SiO ₂ (1% wt.) measured during steady-state HCOOH catalysis (0.84 kPa, 353 K) and in flowing N ₂ (at 353 K) after the removal of HCOOH(g) from the reactant stream. b) Normalized absorbance for infrared bands for HCOOH* (at 1570 cm ⁻¹) on Pd/SiO ₂ (1% wt.) as a function of time in flowing N ₂ (at 353 K); these values are normalized by their steady-state value (t < 0) before flowing N ₂ . Dashed line represents the regression of the data to the first-order decomposition.	29
Figure 3.10.	Dehydrogenation turnover rates of HCOOH, DCOOH, and HCOOD (per surface Pd atom) on Pd/SiO ₂ (1% wt.) as a function of HCOOH pressure (0.17-3.36 kPa; 373 K). Dashed curves represent the optimal regression rates using the functional form of Eq. (3.1).....	30
Figure 3.11.	TPD of HCOOH on Pd/SiO ₂ (1% wt.) showing HCOOH, CO ₂ and H ₂ desorption rate as a function of temperature.....	34
Figure 3.12.	HCOOH dehydrogenation turnover rates (per Pd atom) measured on Pd/SiO ₂ (0.05%, 0.1% and 1% wt.) as a function of HCOOH pressure (0.17-3.36 kPa, 363 K). Dashed curves represent the optimal regression rates using the functional form of Eq. (3.1).....	35
Figure 3.13.	HCOOH dehydrogenation turnover rates (per surface metal) on Au/Al ₂ O ₃ (0.61% wt.), Pd/SiO ₂ (0.1% and 1% wt.) and Pt/Al ₂ O ₃ (2% wt.) as a function of HCOOH pressure (0.17-4 kPa, 353 K). Au/Al ₂ O ₃ and Pt/Al ₂ O ₃ data obtained from Ojeda et al.. Dashed curves represent the optimal regression rates using the functional form of Eq. (3.1) for Pd/SiO ₂ catalyst.	36

LIST OF TABLES

Table 1.1.	Summary of physical and chemical properties of potential H ₂ carriers. (Reproduced with permission from Ref. ¹² , Copyright 2022, Springer Nature)	2
Table 3.1.	Experimental vibrational frequencies of HCOOH gas ^{52,53}	24
Table 3.2.	Equilibrium and rate constants and the corresponding enthalpies and entropies from kinetic analysis.....	33
Table 3.3.	Kinetic isotope effects on equilibrium and rate constants from experiments	33

LIST OF SCHEMES

Scheme 3.1. Proposed sequence of elementary steps for molecular HCOOH dehydrogenation. Quasi-equilibrated steps are denoted by ovals in double arrows.....	31
------------------------------------------------------------------------------------------------------------------------------------------------------------	----

ACKNOWLEDGEMENTS

I would like to acknowledge the support of my thesis advisor Dr. Stephanie Kwon for providing me with so much guidance and support on both my journey to my master's degree. Thank you so much for helping me grow as a researcher and a person. You have always been there to support me with both my technical and personal questions. Thank you for always pushing me to do better.

I would also like to acknowledge the members of the LCAT lab group: Manasi Vyas, Michelle Nolen, Kemakorn Ithisuphalap, and Emily Volk who have always been there for input and advice. I really appreciate them always being there for the millions of questions and terrible jokes.

It is also important to acknowledge the unwavering support of all my friends. Thank you for always encouraging me to follow my passion and be myself. Thank you for the many nights of explaining my research in tedious details so I could practice my public speaking. Thank you for always being there for the moment when I felt defeated and holding me up. Thank you for being my support system.

Lastly, I would like to thank my parents, Nancy and Drew Schlusel. They have literally always been there for me. Thank you for always being there for my random phone calls after meeting with my advisor so I could talk about all the new discoveries and lessons I learned. Thank you for your support as I pursued my master's. I would not be here today if it was not for your encouragement to follow my passion for learning.

CHAPTER 1

INTRODUCTION

1.1. Importance of Hydrogen Storage Technology

Hydrogen (H_2) has emerged as a potential energy source to combat the current environmental and energy crisis due to its high energy density (120 MJ/kg), availability, and clean nature¹. In addition to these properties, it is also a versatile and sustainable energy carrier that can be produced via water (H_2O) electrolysis combined with various renewable electricity sources. It is also highly transportable and environmentally friendly. The combustion of H_2 to produce energy only results in the byproduct of H_2O , making it an excellent clean energy source with minimal to no air pollutants². In contrast to electricity, H_2 can also be stored in various physical and chemical forms³. Thus, green H_2 can play a significant role as we transition to cleaner and more sustainable energy systems.

The safety issues related to the storage and transportation of H_2 have limited the implementation of an H_2 economy. There have been many advancements in H_2 storage techniques, such as compressed H_2 gas, liquid H_2 , H_2 adsorption on nanomaterials, and chemical H_2 storage. Compressed and liquid H_2 storage methods are most often used due to their relatively high H_2 density (70 kg H_2/m^3 at standard temperature and pressure (STP))⁴. However, compressed H_2 requires high-pressure containers that can be expensive to make. Both the compression and liquefaction processes require a large amount of energy to achieve the necessary pressure and cryogenic conditions⁵. Alternative approaches such as H_2 adsorption on high surface area materials (e.g., carbon nanotubes⁶ and metal-organic frameworks (MOFs)⁷) have limited success due to low gravimetric (<2.3 H_2 % wt.) and volumetric (<14.7 kg H_2/m^3) densities at ambient temperatures (~298 K). Some Cu-MOFs have been able to achieve high gravimetric and volumetric densities (9.95 H_2 % wt.; 53 kg H_2/m^3) at low temperatures (~77 K, cryogenic temperature), yet both capacities decreased significantly at higher temperatures (~298 K)⁷⁻⁹. More recently, chemical H_2 storage techniques that utilize hydrogenation-dehydrogenation reactions have emerged as a safe method to store and release H_2 on

demand. Examples of chemical H₂ carriers include methanol (CH₃OH), methyl cyclohexane (CH₃C₆H₁₁), cyclohexane (C₆H₁₂), ammonia (NH₃), and formic acid (HCOOH), all of which remain liquid at room temperature, and offer the benefits of easy transportation and long-term storage without the need for cryogenic devices, high-pressure systems, or gas-pipe lines^{10,11}. Table 1.1 summarizes the physical and chemical properties of the proposed chemical H₂ carriers¹².

Table 1.1. Summary of physical and chemical properties of potential H₂ carriers. (Reproduced with permission from Ref.¹², Copyright 2022, Springer Nature)

H ₂ Carrier	Boiling Point (K)	Density (kg/m ³) ^a	Gravimetric Content (H ₂ % wt.)	Volumetric content (kg H ₂ /m ³) ^b	Flash Point (K)	Ref.
Liquid H ₂	20.3	71	100	70	-	4
Methanol	337.8	790	12.1	100	284	4,13,14
Ammonia	239.8	730	17.8	121	405	4,13,15,16
Methyl Cyclohexane	373.6	770	6.2	47	269	4,13,15
Cyclohexane	353.9	780	7.2	56	253	4,13
Formic Acid	373.9	1,220	4.4	53	342	4,13

^aAt standard temperature-pressure (STP) conditions

^bCalculated from the density of respective molecules at STP

1.2. Formic Acid as a Potential Liquid Hydrogen Carrier

HCOOH is currently considered to be one of the most promising liquid H₂ carriers due to its relatively high H₂ density (4.4 H₂ % wt.; 53 kg H₂/m³; Table 1.1) (higher than the 2020 target of 40 kg H₂/m³ for an on-board H₂ storage for light-duty vehicles by the U.S. Department of Energy (DOE)¹⁷), low toxicity, low flammability, environmentally benign nature, and ease of handling. Its high boiling point (373.9 K¹³) allows it to remain in the liquid phase at ambient temperatures. While cyclohexane, methyl cyclohexane, and methanol have higher gravimetric H₂ densities than HCOOH, they are highly flammable, as indicated by their low flash points (Table 1.1). This renders them unfavorable H₂ carriers, especially considering the need for their long-term storage and transportation. Additionally, benzene, the dehydrogenation product of cyclohexane, is carcinogenic, raising significant health concerns regarding the use of cyclohexane as an H₂ carrier. Ammonia is currently the second most produced chemical in the world through the steam methane reforming (SMR) process and has been recognized as a sustainable H₂ carrier.

However, the production of ammonia uses approximately 2% of global energy produced and generates over 420 million tons of carbon dioxide (CO₂) annually¹⁸. Although green ammonia production is a current research focus in the field of liquid H₂ carriers, green ammonia production as of 2023 remains unsustainable at industrial scale¹⁹. Lastly, current industrial production methods of HCOOH include hydrolysis of methyl formate or formamide and the oxidation of biomass. However, direct hydrogenation of CO₂ to HCOOH has emerged as a viable process to directly use CO₂ emissions with green H₂ to form HCOOH with limited emissions. The viability, advances, and challenges of developing green HCOOH production and other commonly used chemicals have been thoroughly identified in literature²⁰.

HCOOH decomposition can take place by dehydration (CO/H₂O products) or dehydrogenation (CO₂/H₂ products) (Figure 1.1). However, in order to utilize the HCOOH decomposition reaction in sequence with H₂ fuel cells, it is imperative to avoid the dehydration product of CO since it can lead to the poisoning of the catalysts used in fuel cells²¹. It has been reported that formic acid dehydration can be avoided by using highly selective catalysts for dehydrogenation products. Note that the dehydrogenation of HCOOH results in a stoichiometric amount of CO₂ that can be recycled by reacting with green H₂ in HCOOH synthesis to establish a carbon-neutral cycle. Utilizing an active and selective catalyst for the hydrogenation/dehydrogenation cycle at near ambient temperatures could allow for an efficient carbon cycle to produce an energy source with little to no greenhouse gas emissions. This research focuses only on the dehydrogenation part of the cy

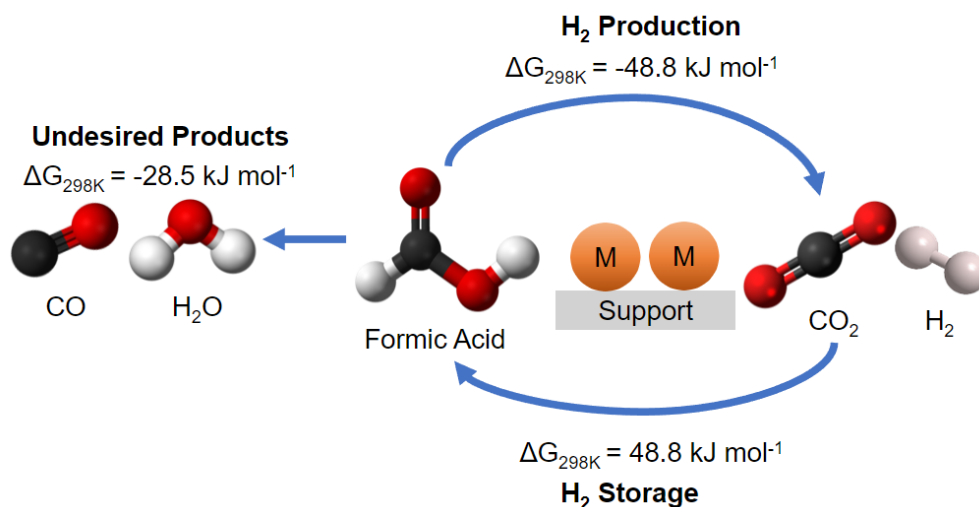


Figure 1.1. HCOOH hydrogenation-dehydrogenation pathway and desired products, based on reported data from Ref.²².

1.3. Metal Based Catalysts for Formic Acid Dehydrogenation

The decomposition of HCOOH over heterogeneous catalysts has been studied since the 1930s. However, initial studies were conducted on the optimization of the catalysts and the measurements of CO evolution from HCOOH dehydration. This led to many studies investigating HCOOH decomposition in the gas phase and temperatures higher than 373 K²³. Transition metals such as copper (Cu), palladium (Pd), platinum (Pt), and gold (Au) have become the most common metals studied in literature. Pt has been suggested as the most active metal for HCOOH dehydrogenation catalysis among the other common transition metals (Figure 1.2); however, Pt has been shown to be highly susceptible to CO poisoning. In their ultrahigh vacuum studies, Columbia et al. that the presence of CO* (>0.4 monolayer (ML)) was capable of completely quenching CO₂/H₂ formation²⁴. Pd, the second most active metal for HCOOH dehydrogenation, is a very promising alternative due to its ability to be more tolerant to CO than other metals²⁵.

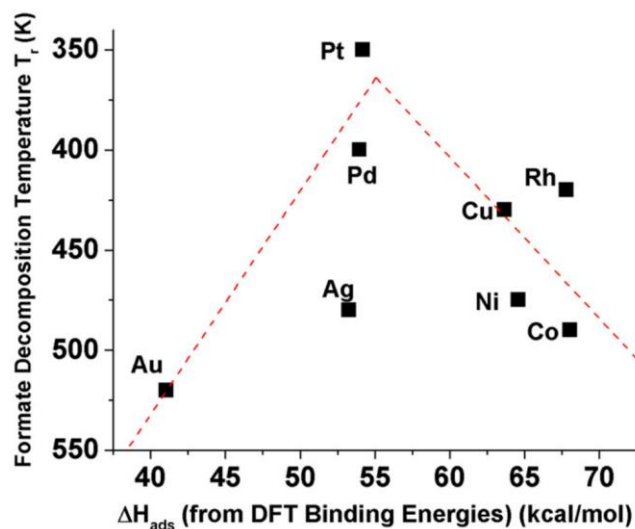


Figure 1.2. Decomposition temperature (T_r (K)) of adsorbed formates on metallic powders from TPD measurements as a function of formate binding energies on metal (111) surfaces from DFT methods. (Reproduced with permission from Ref.²⁶, Copyright 2016, Elsevier)

Pd-based catalysts have received increasing interest over the past few years due to their high reactivity at near ambient temperatures^{26–42}. Most experimental studies have observed more than 90% selectivity towards the dehydrogenation products than the dehydration products (>423 K)^{43–46}. Yet, the identities of reactive intermediates and the elementary steps involved have remained unclear and conflicted. A Pd-based catalyst (Pd/SiO₂) was chosen as the subject of this thesis to provide a deeper understanding of how HCOOH decomposition occurs on the surface of Pd nanoparticles, where SiO₂ is chosen as a supporting material due to its inactive nature for HCOOH decomposition pathways. This thesis aims to provide insight into the catalytic performance and reaction mechanism on a Pd-based catalyst that could facilitate the development of catalytic processes for H₂ storage and utilization. Chapter 2 provides a literature search of HCOOH decomposition pathways on Pd-based catalysts.

1.4. Outline of Thesis

This work combines kinetic, spectroscopic, and isotopic methods to identify and assess the reaction pathway and elementary steps involved in HCOOH dehydrogenation on a Pd/SiO₂ catalyst. This work provides a molecular-level picture of HCOOH

decomposition on Pd/SiO₂ to facilitate the future development of catalytic processes for H₂ storage and utilization. Chapter 2 provides detailed information about the mechanism of HCOOH decomposition on metal surfaces and background for the knowledge gaps associated with Pd-based catalysts for HCOOH decomposition. Chapter 3 discusses the results of the catalytic performance and reaction mechanism on a Pd/SiO₂ catalyst. Kinetic studies are used to estimate rate and equilibrium constants and to propose a potential reaction pathway. Kinetic studies were also used to assess the particle size effects on the rate and equilibrium parameters, CO₂/CO selectivity, and the stability of the catalyst to provide insight into potential catalytic design strategies. Infrared spectroscopy (IR) was utilized to identify the surface species present during the reactions, which helped provide insight into the reaction mechanism and reaction intermediates. Isotopic methods were utilized to estimate a potential reaction pathway by identifying the kinetically relevant steps. Chapter 4 summarizes the main conclusions made in this thesis and the future of this work.

CHAPTER 2

BACKGROUND

2.1. Mechanism of Formic Acid Decomposition on Metal Surfaces

HCOOH decomposition can occur through the dehydrogenation reaction to form CO_2 and H_2 or the dehydration reaction to form CO and H_2O ^{47,48}. The successful utilization of HCOOH as an H_2 carrier in parallel with H_2 fuel cells requires the development of an active, selective, and stable catalyst that can release H_2 on demand at low temperatures (<400 K) without any formation of CO . Catalytic H_2 fuel cells can experience significant inhibition due to CO poisoning even at ppm levels of CO ⁴⁹. This requires the developed catalysts to experience higher than 99% selectivity towards CO_2 .

The HCOOH decomposition reactions on metal catalysts have been widely studied to understand the surface properties of these catalysts. From these studies, it was found that HCOOH reactions can involve either formate (HCOO^*) or carboxylate (COOH^*) intermediates that form from either the activation of the O-H or C-H bonds in HCOOH (Figure 2.1). Formates can form either in the bidentate configuration on two vicinal metal atoms (HCOO_B^*) or in the monodentate configuration on one metal atom (HCOO_M^*)^{47,48}. Both HCOO^* intermediates can result in CO_2 products due to a subsequent C-H activation, resulting in the H-atoms (H^*) being released as $\text{H}_2(\text{g})$ through re-combinative H_2 desorption. Alternatively, COOH^* intermediates can lead to CO_2 products by cleaving its O-H bond or to the CO products by activating the C-O bond, leading to the OH^* recombining with H^* to form H_2O . The abundance of HCOO^* and COOH^* pathways and CO_2/CO selectivity heavily depend on the nature and identity of the catalyst used.

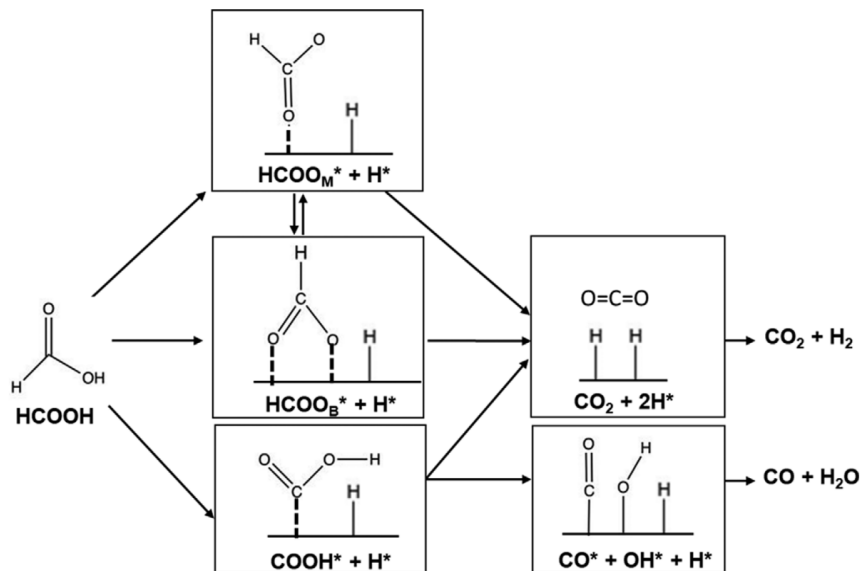


Figure 2.1. Schematic of HCOOH decomposition pathways on transition metal surfaces, based on the proposed mechanisms discussed in Ref.^{47,48}. (Reproduced with permission from Ref.¹², Copyright 2022, Springer Nature)

A Pd-based catalyst was chosen due to its high catalytic activity and selectivity at low temperatures. However, many gaps exist in literature around the viability, and stability of Pd-based catalysts for HCOOH decomposition. Additionally, conclusions about the reaction intermediates and elementary steps are conflicted. The next section goes into depth about what exactly is known and unknown about Pd catalysts for HCOOH decomposition.

2.2. Formic Acid Decomposition Routes on Palladium Based Catalysts

The type of reaction intermediates and elementary steps observed on Pd-based catalysts have been shown to be conflicting in literature. Jorgensen and Madix found in their electron energy loss spectroscopy (EELS) that at 80 K, HCOOH binds molecularly to clean Pd(100) surfaces. There were no formate or carboxylate species detected when the sample was heated to 170 K. It was observed that the molecularly bound HCOOH species would partially desorb as gas phase HCOOH while any remaining HCOOH would decompose to form CO products that desorbed around 515 K with no detectable formation of CO_2 ³². In contrast, Davis and Barteau reported observing formates forming on the surface of clean Pd(111) surfaces around 200 K during high-resolution electron energy loss spectroscopy (HREEL)³³. Temperature programmed deposition (TPD)

analysis found that the formate species would decompose, forming CO₂ (~260 K), H₂ (~330 K), and CO (~490 K) with a CO₂/CO selectivity of 1.6. Density functional theory (DFT) calculations conducted on Pd(111) and Pd(100) surfaces at low coverage limits ($\leq 1/9$ ML) suggested that HCOOH dehydrogenation can occur via both HCOO_B* and COOH* intermediates, with only the latter leading to CO products (Figure 2.2)^{34–36}. These results contradict the spectroscopic studies where formate species were the only observed intermediates^{26,32}. These discrepancies were proposed to be due to the presence of co-absorbed species that could impact the reaction mechanism and stability of bound intermediates. Davis and Barteau's vibrational spectra experiment showed that CO* and O* species can co-exist with formates on the Pd(111) surface during decomposition reactions³³. Computational work by Li et al. showed that the presence of 0.55 CO* ML rendered the HCOO_B* pathway unfavorable on both Pd(100) and Pd(111) surfaces. Instead, the reaction would proceed through the COOH* pathway, leading to the formation of CO products on Pd(111) and CO₂ products on Pd(100)³⁶. The varying products on the different surfaces showed the importance of the structure sensitivity of the Pd-based catalyst. It remains unclear why the theoretical and experimental studies come to different conclusions on the reactive intermediate of HCOOH decomposition on the Pd catalysts. Experimental studies suggest either molecular HCOOH or HCOO* to be the relevant intermediates, while theoretical studies suggest HCOO_B* and COOH*. The varying conditions and Pd surfaces used make it difficult to draw a conclusion on the type of intermediates observed.

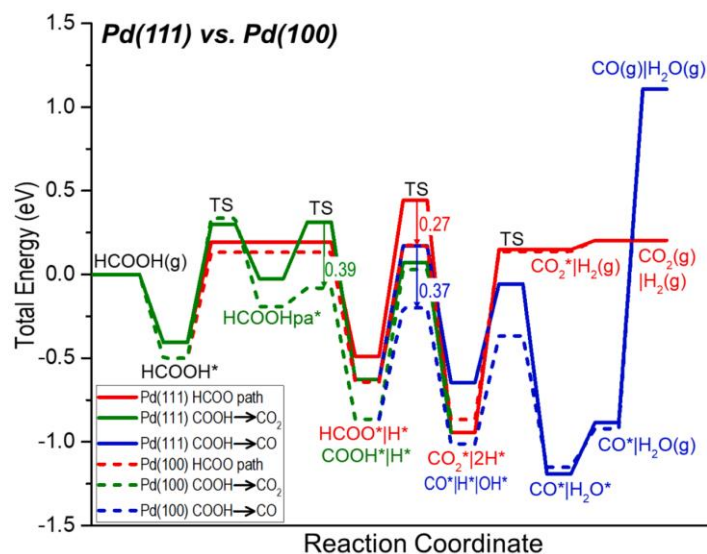


Figure 2.2. DFT-derived energy (eV) of reactive intermediates and transition states involved in HCOO* and COOH* pathways on Pd(100) (solid lines) and Pd(111) (dashed lines) surfaces. The arrows show the downshift in transition state energy on Pd(100) compared to Pd(111). (Reproduced with permission from Ref.³⁶, Copyright 2021, Elsevier)

Several studies have investigated the impact of Pd nanoparticle size on the rate of HCOOH dehydrogenation reaction. These studies have consistently concluded that as the size of the Pd nanoparticles decreases, the catalytic activity increases. Kim et al. observed a nearly linear relationship between the apparent activation energy for HCOOH dehydrogenation on Pd/C and the average Pd size (estimated from TEM images). This led to higher reaction rates for the smaller Pd particles (Figure 2.3). Kim et al. attributed this size-dependent trend to the challenge of H₂ desorption from larger Pd clusters, as shown in their TPD profiles of size-controlled Pd/C catalysts after reduction at 373 K (Figure 2.3)⁵⁰. Li et al. corroborated these findings, reporting a significant increase (by a factor of 3.6) in catalytic rates as Pd particle size decreased from 4.5±0.5 to 2.1±0.3nm (estimated from scanning transmission electron microscopy, STEM)³⁶. They proposed that smaller Pd particles offer higher Pd dispersion and a more significant proportion of positively charged Pd species than of metallic Pd based on their ex-situ X-ray photoelectron spectroscopy (XPS) measurements.

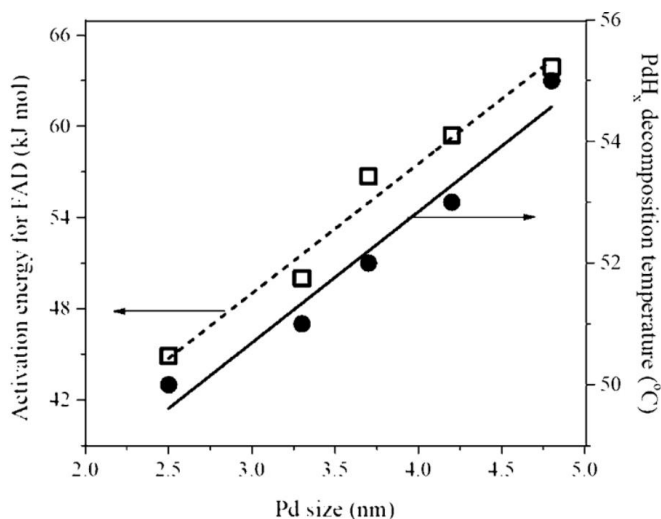


Figure 2.3. Apparent activation energy of HCOOH dehydrogenation (1 M HCOOH in H₂O; 303-333 K) on Pd/C (left axis) and the decomposition temperature of PdH_x, measured from TPD analysis after reduction of Pd/C at 373 K in H₂ (the right axis) as a function of average Pd sizes (from TEM images) (Reproduced with permission from Ref.⁵⁰, Copyright 2019, Elsevier)

The stability of Pd catalysts during HCOOH reactions in aqueous solutions has also been discussed in literature, to ensure potential use of the catalyst in industrial applications^{29,30,41}. Kim et al. reported that supported Pd catalysts showed complete deactivation after the third use without a regeneration process involving washing and drying between runs. The deactivation was attributed to the deposition of species derived from reactants/products on the Pd surfaces²⁹. Early work by Ruthven and Upadhye suggested that the deactivation of Pd black catalysts during HCOOH decomposition in aqueous solutions resulted from the accumulation of hydrogen atoms (H*) on the Pd surface, based on their kinetic analysis⁴¹. Hu et al. demonstrated that the reactivity of Pd/C catalysts could be fully restored by drying the used catalysts at 383 K. This led the authors to propose that deactivation if not due to the agglomeration or loss of active Pd sites in the solution³⁰. Hu et al. performed TPD analysis on the used catalysts with an online mass-spectrometer to show the absence of CO evolution, indicating that CO* was not the source of deactivation. Instead, they observed the evolution of H₂ and CO₂. From this, they proposed that the deactivation could be caused by the formation of HCOO* species on the Pd surfaces that cannot decompose at low operating temperatures. However, whether it is HCOO* or COOH* species cannot be confirmed without

spectroscopic evidence. Overall, the proposed deactivation mechanisms vary, with suggestions ranging from the accumulation of hydrogen atoms on Pd surfaces to the formation of species that cannot easily decompose at the operating temperature. Understanding these deactivation processes is essential for optimizing and extending the use of Pd catalysts in practical applications. This thesis will focus on filling the gaps in literature for the gas-phase reaction of HCOOH dehydrogenation on a Pd/SiO₂ catalyst.

CHAPTER 3

FORMIC ACID DECOMPOSITION PATHWAYS ON SUPPORTED PALLADIUM NANOPARTICLES AT NEAR AMBIENT TEMPERATURES

3.1. Introduction

HCOOH has been proposed as a potential liquid H₂ carrier because of its relatively high H₂ density (4.4 H₂ % wt.; 53 kg H₂/m³), high boiling point (373.9 K), low toxicity, environmentally benign nature, low flammability, and ease of handling¹³. HCOOH decomposition can occur via dehydrogenation (to CO₂/H₂) or dehydration (CO/H₂O) pathways, where the selectivity between the two pathways depends on the nature and type of catalysts and the operating conditions. To successfully commercialize HCOOH dehydrogenation, the development of an active, selective, and stable catalyst that releases H₂ at near-ambient conditions without the formation of carbon monoxide (CO) is required. The formation of CO can limit the use of the H₂ product stream due to CO poisoning of H₂ fuel cells. For example, Pt-based fuel cells have shown significant inhibition in the presence of even 10 ppm levels of CO⁴⁹. Therefore, developing a catalyst that does not produce any CO products is important.

Pd-based catalysts have received much interest for their use in HCOOH dehydrogenation due to its high reactivity near ambient temperatures²⁶⁻⁴². The types of reaction intermediates and elementary steps of HCOOH dehydrogenation on Pd surfaces have remained conflicted in literature. EELS experiments on clean Pd(100) surfaces at 80 K showed that HCOOH bound molecularly without detecting bound formate species when the sample was heated to 150 K. The molecularly bound species partially desorbed as gas-phase HCOOH while any remaining HCOOH decomposed to form CO products³². Monodentate formates (HCOO_M*) were only found to form on O*-covered Pd(100) surfaces that further decomposed to CO₂ products at 265 K. H₂ evolution occurred around 340 K with the rate limited by the desorption step. A HREEL study reported HCOOH dissociating to form formates on clean Pd(111) around 200 K. TPD analysis showed the

formates decomposing at higher temperatures to form CO₂ (~260 K), H₂ (~330 K) and CO (~490 K) with a CO₂/CO selectivity of 1.6³³. DFT calculations on these same surfaces (Pd(100) and Pd(111)) at low surface coverage ($\leq 1/9$ ML) showed that HCOOH dehydrogenation can proceed through both the bidentate formate (HCOO_B^{*}) or the carboxylate (COOH^{*}) intermediates. The COOH^{*} intermediates were the only intermediate that resulted in CO products. The contradiction between the theoretical and experimental studies makes it difficult to determine how exactly HCOOH decomposes on Pd-based catalysts near ambient temperatures. Overall, molecularly bound HCOOH, HCOO_M^{*}, HCOO_B^{*}, and COOH^{*} were all observed in literature as potential intermediates for HCOOH dehydrogenation on Pd surfaces.

Several works have reported the importance of the particle size effects of the Pd nanoparticles for the HCOOH dehydrogenation rate. All showed a similar trend where the rate increased with decreasing particle size. Kim et al. showed that the apparent activation energy for HCOOH dehydrogenation on Pd/C catalysts scaled almost linearly with the average Pd size, leading to higher turnover rates for the smaller Pd particles. This trend was attributed to the difficulty of H₂ desorption on large clusters⁵⁰. Li et al. also found that the catalytic rates increased by a factor of 3.6 when particle sizes decreased from 4.5 +/- 0.5 to 2.1 +/- 0.3 nm³⁶.

While there has been significant progress made in understanding the behavior of Pd-based catalysts for HCOOH dehydrogenations, some aspects remain unknown or require further investigation, specifically for Pd/SiO₂ catalysts. There is a limited amount of literature investigating the reaction kinetics and mechanism of HCOOH dehydrogenation on Pd/SiO₂ catalysts. While there have been multiple reported observed intermediates that can occur on Pd nanoparticles, it is unknown which intermediate, and pathway will occur on the Pd/SiO₂ catalysts. SiO₂ is a known inert support for this reaction and is known to be good with H₂ adsorption, which could benefit the overall reaction. This research investigated the kinetics and mechanism of HCOOH dehydrogenation on Pd/SiO₂ catalysts while also investigating the size dependence of Pd nanoparticle supported on SiO₂ and how it affects the overall reaction.

This work combines kinetic, isotopic, and spectroscopic analysis to evaluate and identify the plausible mechanisms that describe the dehydrogenation reaction on the Pd surfaces. The purpose of this study is to provide an in-depth analysis of HCOOH dehydrogenation on a Pd/SiO₂ catalysts to fill in the gaps in current literature and promote further investigation into the viability of Pd/SiO₂ catalysts for the potential use in H₂ storage technologies. This work's results and conclusions can be utilized to aid in catalytic design strategies to improve catalytic performance by providing insight into the reaction kinetics and elementary steps of HCOOH dehydrogenation on Pd nanoparticles at near ambient temperatures.

3.3. Methods

3.3.1. Catalyst Preparation and Characterization

The Pd/SiO₂ catalyst (0.01-1% wt.) was prepared via strong electrostatic adsorption of Pd precursors onto a silica support, followed by reduction, and passivation to form metallic clusters. This synthesis method was adopted from the method reported by N. M. Wilson and D. W. Flaherty⁵¹. Silica (15 g, Sigma-Aldrich, DAVISIL 646, 35-60 mesh) was added to 300 cm³ of DI water, followed by the addition of 30 cm³ of 14.5 NH₄OH (Macron, 28-30 wt%) to obtain a pH greater than 11. In a separate beaker, 0.346 g of Pd(NH₃)₄Cl₂ (Sigma Aldrich, >= 99.99%) was added to 15 cm³ of DI water. The solution was added dropwise to the basic solution containing silica. The resulting solution was stirred for 3 hours and then vacuum-filtered to recover the solids. The recovered solids were rinsed with an additional 500 cm³ of DI water and vacuum filtered again. The rinsed solids were dried for 24 hours at 353 K in stagnant air. The dried solids were then heated to 573 K (3 K/min) and held at 573 K for 4 hours in 20 mol% H₂ and 80 mol% He at 100 cm³/min to reduce the Pd to metallic nanoclusters in a reductive treatment and achieved theoretical particle size of 0.7 nm, as reported previously by Wilson and Flaherty⁵¹. No ex-situ oxidative treatment was used within the scope of this work. Finally, the catalyst was passivated at ambient temperature by flowing 500 cm³/min of 4 mol% O₂ and 96 mol% He for 0.5 hours. Once the sample was finished with ex-situ treatments, the

sample was sieved to achieve aggregate particles sizes < 75 μm , 180-125 μm , and 250-180 μm .

3.3.2. In-Situ Infrared Spectroscopy

In-situ infrared spectra were collected in transmission mode using a Nicolet iS50 FT-IR (Thermo Fisher) spectrometer. Pd/SiO₂ samples were pressed into self-supporting wafers (10-30 mg) and loaded into a stainless steel, high-temperature cell (Harrick Scientific Products) with NaCl windows. The temperature was maintained using external resistive heating, monitored with a thermocouple (K-type, Omega) that was held at the outer reactor wall near the outer edge of the wafer and controlled with an electronic temperature controller (Harrick Scientific Products, Watlow EZ-ZONE). The cell was cooled with a chiller (Neslab Coolflow CFT-25). Inlet flow rates were controlled by mass flow controllers (He (Parker; Series 2), H₂ (Brooks; Series 5850E)) and adjusted to maintain a target flow rate and pressure of N₂ (General Air; 99.999%) and H₂ (General Air; 99.999%). HCOOH (Sigma-Aldrich; >90%; used without further purification) was introduced to the system as a liquid into a flowing gas stream using a syringe pump (KD Scientific; Series 200347) and vaporized at 323 K. All the transfer lines, except for the one near the injection port, were kept at ambient temperature to prevent HCOOH decomposition within the lines. HCOOH pressures were also kept below its vapor pressure at ambient temperatures (5.3 kPa at 298 K) to prevent condensation within the unit.

The Pd/SiO₂ wafers were pretreated in 20% H₂/N₂ (100 ml/min) by heating the temperature to 573 K at 3 K/min and held for 1 hour before being cooled down to reaction temperature (353-423 K). The system was flushed with N₂ (100 ml/min) at the reaction temperature to collect background spectra before introducing HCOOH into the system. The amount of HCOOH flowed was adjusted between 0.17-3.36 kPa HCOOH with the equivalent amount of He (100 ml/min total flow). All spectra were collected at a resolution of 4 cm⁻¹ and averaged 64 scans during the HCOOH reaction and 4 scans during the N₂ flush from 4000-400 cm⁻¹.

Infrared spectroscopy was used to gain insights into the identity and surface coverage of bound species during HCOOH dehydrogenation. The change in the intensity of peaks not corresponding to known reactants and products was monitored after HCOOH was introduced over a range of varying pressures to determine the surface intermediates and associated equilibrium constants.

3.3.3. Kinetic Analysis

Catalytic HCOOH decomposition rates (0.2-4 kPa HCOOH, 353-383 K) were measured on Pd/SiO₂ samples. The catalyst samples (~0.01 g) were held within a U-shaped quartz reactor (4 mm inner diameter), and the ends of the reactor were cushioned with quartz wool to prevent any catalyst from entering the reactor unit. The reactor's temperature was measured using a thermocouple (K-type) wrapped around the reactor and controlled with an electronic temperature controller (Fe e-Front runners; Model PXR3). The quartz wool did not give any detectable reaction rates at any conditions of the catalytic experiment.

All Pd samples were pretreated in 20% H₂/He (100 ml/min) by heating to 573 K at 3 K/min and held for 1 hour before cooling down to reaction temperature (353-423 K). The system was then flushed with He (100 ml/min) for at least 30 minutes at the reaction temperature before introducing HCOOH to the system. Inlet flow rates were controlled using individual mass flow controllers (mks; IO Type B) and adjusted to ensure molar flow rates of He, H₂, and Ar (General Air; 99.999%). HCOOH and its isotopes (DCOOH and HCOOD, Cambridge Isotope Laboratories; >98% chemical and isotopic purities for both) were introduced to the system as a liquid into a flowing gas stream using a syringe pump (KD Scientific; Series 200347) and vaporized at 323 K. All the transfer lines, except for the one near the injection port, were kept at ambient temperature to prevent HCOOH decomposition within the lines. HCOOH pressures were also kept below its vapor pressure at ambient temperatures (5.3 kPa at 298 K) to prevent condensation within the unit. The concentrations of the reactant (HCOOH and its isotopes), products (H₂ and CO₂), and CO in the product stream were measured using a mass spectrometer with a detection limit of <100 ppb for non-interfering species (MKS Spectra; Cirrus 2).

3.3.4. Temperature Programmed Desorption (TPD)

The TPD measurements were performed in the same reactor with the same setup discussed above. The Pd/SiO₂ samples were sieved between 125-180 μm aggregate diameters and loaded into a U-shaped quartz reactor (~0.5 g). The sample was pretreated in 20% H₂/He (100 mL/min) at 573 K (3 K/min) for 1 hour before being cooled down to 303 K. After cooling down the system, the catalyst was flushed with flowing He for 1 hour to remove any physically adsorbed gases. Then, 0.336 kPa HCOOH in He (100 ml/min) was introduced for 1 hour. After HCOOH adsorption, the sample was purged with flowing He for 1 hour to remove residual HCOOH. The TPD was performed by heating the sample to 573 K (3 K/min) in flowing He (100 mL/min), and the desorbing molecules were monitored with the attached mass spectrometer.

3.4. Results and Discussion

3.4.1. Formic Acid Decomposition Rates, Selectivities, and Stabilities on Pd/SiO₂

Figure 3.1. shows HCOOH dehydrogenation rates (per surface Pd atom) measured on Pd/SiO₂ (1% wt.) as a function of time-on-stream (0.84 kPa HCOOH, 383 K). CO₂/H₂ were the only products measured while the production of CO/H₂O was below the detection limit of 100 ppb. No apparent deactivation was observed up to 60 ks, indicating the viability of Pd-based catalysts for selective HCOOH dehydrogenation.

Literature has shown that Pd-based catalysts for HCOOH decomposition can result in either dehydrogenation (CO₂/H₂) or dehydration (CO/H₂O) products^{34–36}. For example, Bulushev et al. have reported a 99% selectivity towards dehydrogenation products on 10% wt. Pd/C (2.4 kPa HCOOH, 403 K)⁴⁴. However, Solymosi et al. have observed both dehydrogenation (90-95% selectivity) and dehydration products on Pd/Norit with decreasing selectivity at higher temperatures (5 kPa HCOOH, 523-623 K)⁴³. Note that literature observes both decomposition products at temperatures greater than 400 K; this research explores the selectivity of Pd/SiO₂ at temperatures less than 383 K.

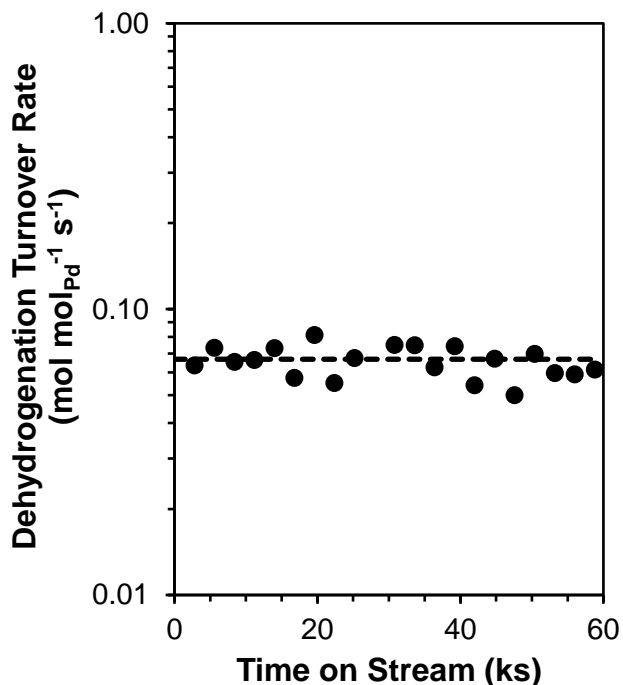


Figure 3.1. HCOOH dehydrogenation turnover rate (per surface Pd atom) measured on Pd/SiO₂ (1% wt.) as a function of time on stream (0.84 kPa HCOOH, 383 K). Dashed line represents the trend line.

These results, suggest that a Pd/SiO₂ catalyst is a viable choice for HCOOH dehydrogenation with its ability to be reactive and stable at low temperatures (~383 K). Moreover, its ability to form CO-free H₂ streams makes it attractive for low-temperature fuel cell applications. In the following sections, we discuss details of the proposed reaction mechanisms based on our kinetic, isotopic, and spectroscopic results.

3.4.2. Reaction Kinetics

HCOOH dehydrogenation rates were measured on 1% wt. Pd/SiO₂ catalyst over a range of HCOOH pressures (0.1-3.5 kPa) and reaction temperatures (353-383 K) (Figure 3.2)). The rates increased linearly at low HCOOH pressures and reached asymptotic values at high pressures. The transition from the first-order reaction to a zeroth-order reaction occurred at higher pressures at higher reaction temperatures. The addition of H₂ to the inlet stream did not significantly influence the reaction rates at both high and low HCOOH pressures (Figure 3.3). The observed kinetic behavior was best described by the following equation (Langmuir Equation):

$$rate = \frac{\alpha P_{HCOOH}}{1 + \beta P_{HCOOH}} \quad (3.1)$$

As shown by the dashed lines in Figure 3.2, the chemical understanding of α and β constants requires an investigation into the reaction elementary steps that can be derived from isotopic and spectroscopic methods as discussed in the following sections.

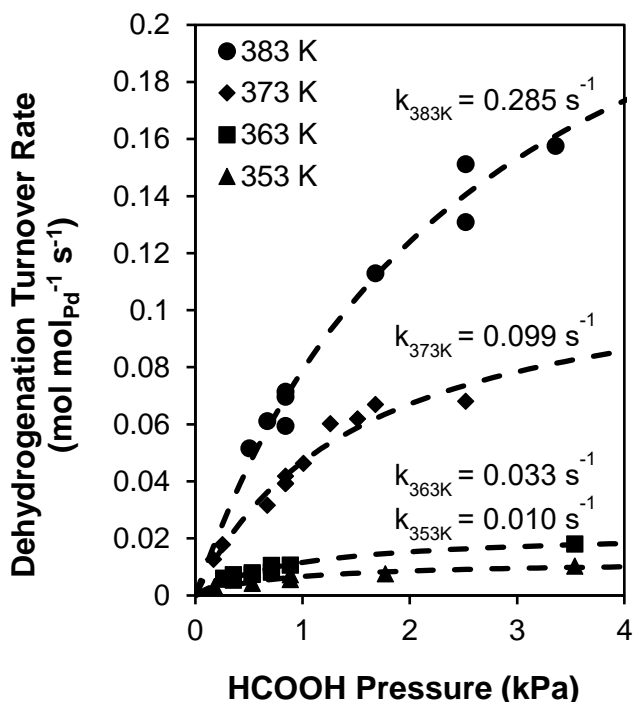


Figure 3.2. HCOOH dehydrogenation turnover rates (per surface Pd atom) measured on Pd/SiO₂ (1% wt.) as a function of HCOOH pressure at a range of temperatures (0.17-3.36 kPa; 353-383 K). The dashed curves represent the optimal regression rates using the functional form of Eq. (3.1).

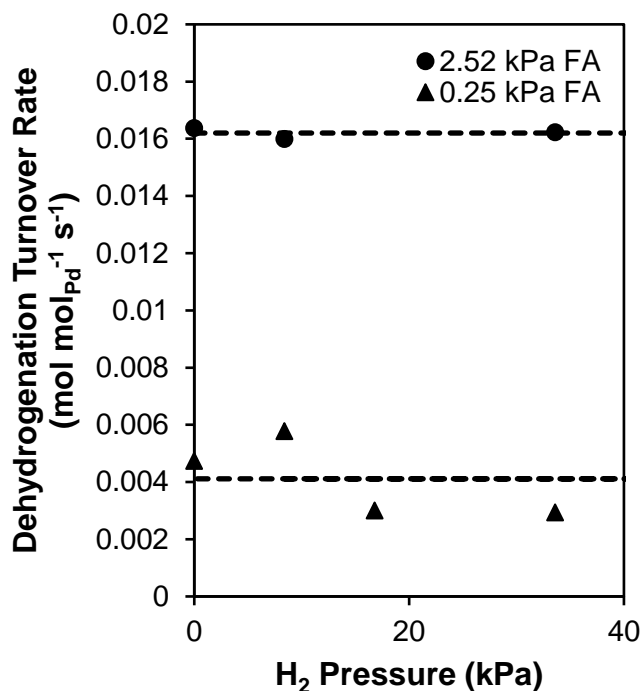


Figure 3.3. HCOOH dehydrogenation turnover rates (per surface Pd atom) measured with H₂ co-feed on Pd/SiO₂ (1% wt.) as a function of H₂ pressure (0-33.6 kPa H₂, 0.25 and 2.52 kPa HCOOH; 363 K). Dashed lines represent the trend lines.

Note that the kinetic data shown in Figures 3.1-3.3 and 3.6-3.13 used 1% wt. Pd/SiO₂ with an aggregate size of 180-125 μm. However, measured rates are independent of aggregate sizes, as shown by the rates that remain essentially unchanged as we vary the average aggregate sizes from 37.5 to 215 μm, indicating that the reaction was not diffusion-limited (Figure 3.4).

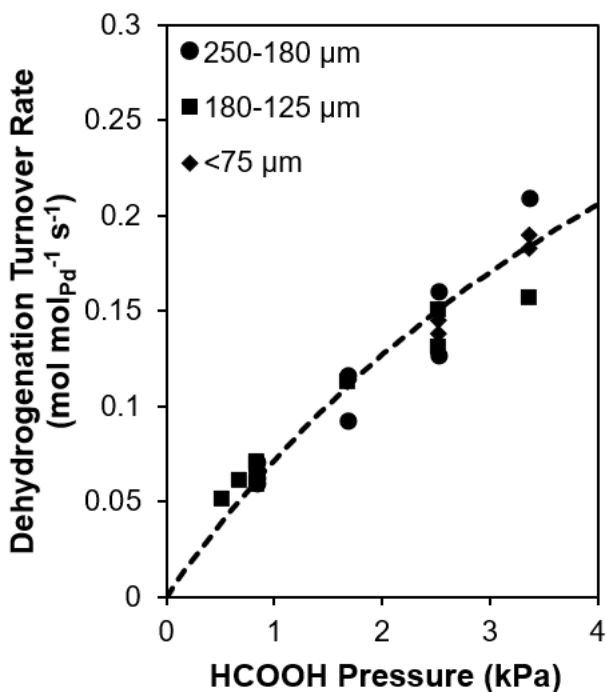


Figure 3.4. HCOOH dehydrogenation turnover rates (per surface Pd atom) measured on Pd/SiO₂ (1% wt.) as a function of HCOOH pressure for varying aggregate sizes (0.17-3.36 kPa; 383 K). Dashed curves represent the optimal regression rates using the functional form of Eq. (3.1).

3.4.2.1. Spectroscopic analysis of surface-bound intermediates

In-situ infrared spectroscopy was utilized to determine the identity of surface species on the Pd nanoparticles during HCOOH decomposition. Table 3.1 summarizes the experimental IR band positions of gas-phase trans HCOOH^{52,53}. There are multiple proposed intermediates for the HCOOH dehydrogenation pathway, including HCOOH*, COOH*, HCOO_M*, and HCOO_B*. Li et al. have reported from DFT calculations that HCOOH decomposition on both Pd(100) and Pd(111) can occur via HCOO_B* and COOH* intermediates³⁶. Bulushev et al. have suggested in their study (Pd/C, 373 K) that the reaction proceeds through an HCOO* pathway⁴⁴. Figure 3.5 provides the DFT-derived spectra for HCOOH* (3014, 2738, 1624, 1288, 1140, and 650 cm⁻¹), COOH* (3510, 1220, 1130, and 680 cm⁻¹), HCOO_M* (1678, 1135, and 682 cm⁻¹), and HCOO_B* (2949, 1291, and 735 cm⁻¹) on the (111) surface of Pd (provided by Michelle Nolen).

Table 3.1. Experimental vibrational frequencies of HCOOH gas ^{52,53}.

Assignment	Wavenumber (cm ⁻¹)
OH stretch	3750
CH stretch	2943
C=O stretch	1770
CH bend	1387
OH bend	1229
CO stretch	1105
CH bend	1033
OCO deform	625

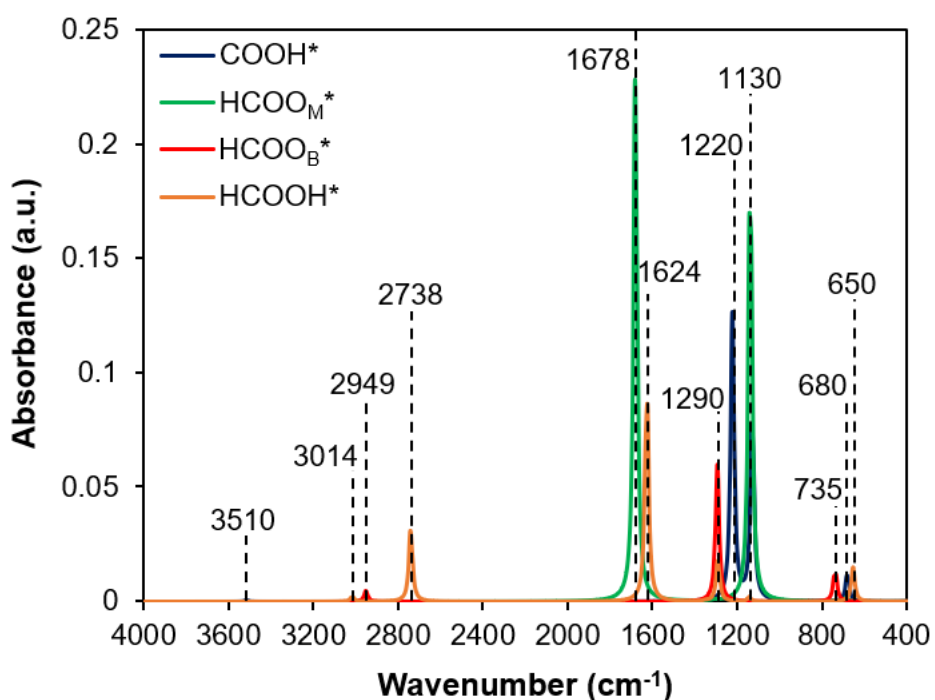
**Figure 3.5.** DFT-derived infrared spectra (PBE-D3) of HCOOH*, HCOO_M*, HCOO_B* and COOH* on Pd(111) surface (provided by Michelle Nolen).

Figure 3.6a depicts the infrared spectra of 1% wt. Pd/SiO₂ samples during HCOOH dehydrogenation over a range of HCOOH pressures (0.17-3.36 kPa; 353 K). Figure 3.6b provides a closer view of the spectra over a wavenumber range. We would expect to see distinct peaks indicating intermediate species. Strong infrared bands are present at 1790,

1747, 1364, 1211, 1118, and 1090 cm^{-1} . A weak band is present at 1570 cm^{-1} , which can be more clearly indicated during the N_2 flush in Figure 3.9a.

The peaks located at 1790, 1747, 1364, 1211, 1118, and 1090 cm^{-1} were found to be associated with $\text{HCOOH}(\text{g})$, leaving only the peak at 1570 cm^{-1} to be associated with an HCOOH -derived intermediate^{52,53}. The peaks associated with COOH^* (1220 and 1130 cm^{-1}), HCOO_M^* (1678 and 1135 cm^{-1}) and HCOO_B^* (1291 cm^{-1}), as indicated by DFT-derived spectra (Figure 3.5) and experimental literature^{54,55}, are not observed. Based on these observations, we hypothesize that HCOOH dehydrogenation proceeds via an HCOOH^* intermediate at these operating conditions.

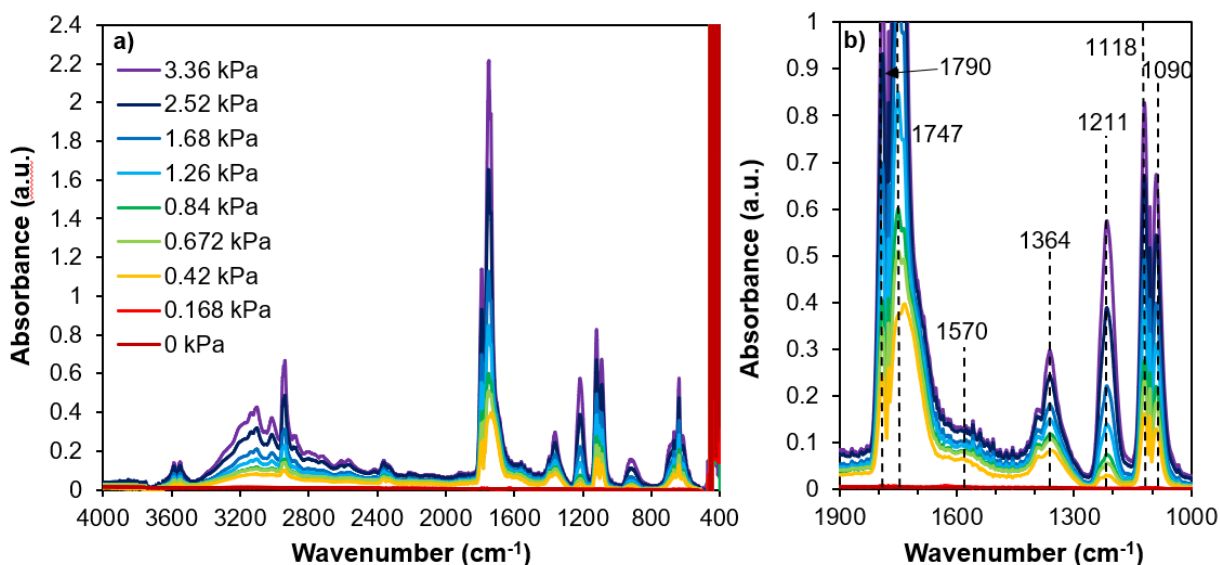


Figure 3.6. (a) Infrared spectra of Pd/SiO_2 (1% wt.) measured during steady-state HCOOH catalysis (0.17-3.36 kPa; 353 K). (b) 1000-1900 cm^{-1} section of spectra labelled with significant bands ($\text{HCOOH}(\text{g})$ (1790, 1747, 1364, 1211, 1118 and 1090 cm^{-1}) and HCOOH^* (1570 cm^{-1})).

Additionally, in-situ infrared spectroscopy was utilized to confirm the presence of CO_2 formation and the absence of CO . Figure 3.7 shows the wavenumber range we would expect to see the distinct peaks indicating CO_2 , CO , and adsorbed CO (CO^*) (highlighted respectively). The infrared bands for CO_2 (2360 and 2340 cm^{-1}) are clearly present, indicating the formation of CO_2 as the primary product. The formation of CO has been confirmed to be lower than 100 ppb levels due to the detection limitations of the mass spectrometer. The clear and distinct peaks for $\text{CO}(\text{g})$ (2180 and 2100 cm^{-1}) and CO^* (2065 cm^{-1}) are not detected, confirming our conclusion that CO does not form at

these conditions (~353 K). The binding energy of CO is very strong (-1.96 eV, hcp, Pd(111)⁵⁶), indicating that if CO was present, we would observe both strong bands associated with CO(g) and CO*. The peaks present at 2211 and 2180 cm⁻¹ are proposed to be due to the C-O stretching of HCOOH on SiO₂.

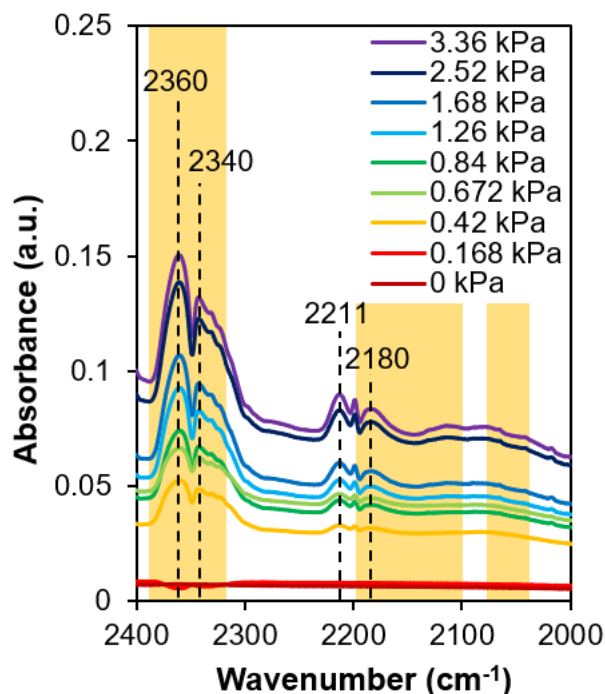


Figure 3.7. Infrared spectra of Pd/SiO₂ (1% wt.) measured during steady-state HCOOH catalysis (0.17-3.36 kPa; 353 K). Significant bands are labelled (CO₂ (2360 cm⁻¹, 2340 cm⁻¹)) and expected band area of CO (2180 cm⁻¹, 2100 cm⁻¹) and CO* (2065 cm⁻¹) are highlighted.

The intensities of the bands for HCOOH (1790 and 1747 cm⁻¹), HCOOH* (1570 cm⁻¹), and CO₂ (2360 and 2340 cm⁻¹) are plotted in Figure 3.8 as a function of HCOOH pressure. Note that these spectra were collected with the same range of HCOOH pressures from the kinetic analysis to observe the surface intermediate covering the surface and calculate an associated adsorption constant by using Equation 3.2 (θ_A is the fractional coverage of HCOOH*, P_{HCOOH} is the partial pressure of HCOOH, and K_{ads} is the equilibrium constant).

$$\theta_A = \frac{K_{ads} * P_{HCOOH}}{1 + K_{ads} * P_{HCOOH}} \quad (3.2)$$

The absorbance of HCOOH follows a linear trend with increasing HCOOH pressure, confirming that HCOOH concentration was increasing as expected in the IR system. The formation of CO₂ follows the same trend observed in the kinetic data, which supports the conclusion that the formation of CO₂ is limited by the presence of a HCOOH-derived intermediate saturating the surface of the catalyst at higher HCOOH pressures. The normalized infrared intensity of HCOOH* also follows the same trend observed during kinetic analysis, supporting the conclusion that HCOOH* is the rate-limiting reaction intermediate and saturates the surface of the catalyst at higher HCOOH pressures. From fitting Equation 3.2 to the experimental data, the K_{ads} was found to be 95. The adsorption constant derived from the kinetic data at the same temperature was found to be 136 which is consistent with the K_{ads} constant found.

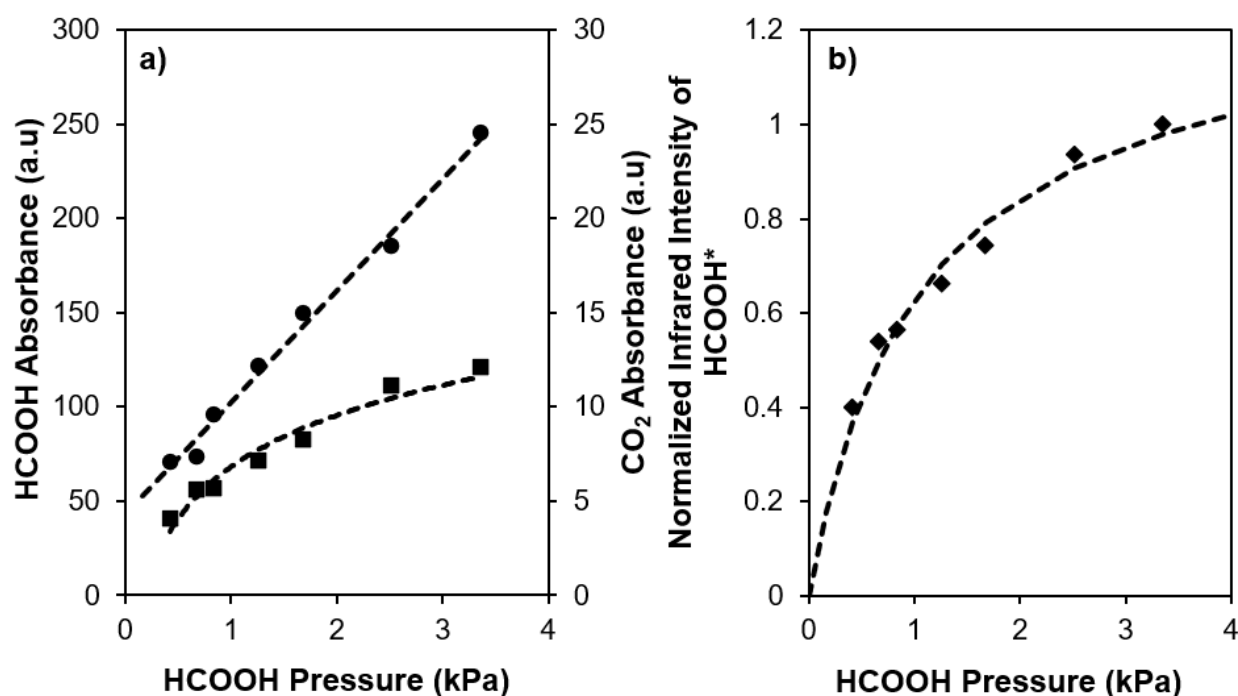


Figure 3.8 (a) Absorbance of HCOOH(g) and CO₂(g) on Pd/SiO₂ (1% wt.) measured during steady-state HCOOH catalysis (0.17-3.36 kPa HCOOH, 353 K). The dashed lines represent the trend lines. **(b)** Surface coverage ratio of HCOOH* band on Pd/SiO₂ (1% wt.) measured during steady-state HCOOH catalysis (0.17-3.36 kPa HCOOH, 353 K). Dashed curve represents the optimal regression of the rate using the functional form of Eq. (3.2).

The intensities of the infrared bands at 1747 cm^{-1} (HCOOH(g)) and 1570 cm^{-1} (HCOOH^*) were monitored at isothermal conditions (353 K) as a function of time elapsed after the removal of HCOOH(g) (0.84 kPa) from the reactant stream (Figure 3.9a). The presence of both bands, even after 0.38 ks, suggests that both species are strongly bound to the surface of the catalyst. A previous study conducted on Cu-based catalysts found that the 1747 cm^{-1} band is due to strongly physisorbed HCOOH on the SiO_2 surface⁵⁷. The 1570 cm^{-1} peak indicates strongly adsorbed HCOOH^* on the surface of the Pd. Note that the 1570 cm^{-1} peak is much more apparent during the N_2 flush than during the steady-state HCOOH dehydrogenation reaction. This is due to the tail of the HCOOH(g) band at 1747 cm^{-1} overlapping with the 1570 cm^{-1} band. Figure 3.9b shows the normalized absorbance of the 1570 cm^{-1} peak over time to obtain the first-order rate constants for the decomposition of the HCOOH^* species. The data was regressed assuming first-order decomposition kinetics (dashed lines). The data follows an accurate regression of the first-order decomposition kinetics after the first 0.1 ks, indicating that the system was flushed entirely of HCOOH(g) . The rate constant for HCOOH^* decomposition obtained from the band intensities after 0.1 ks is 0.0017 s^{-1} .

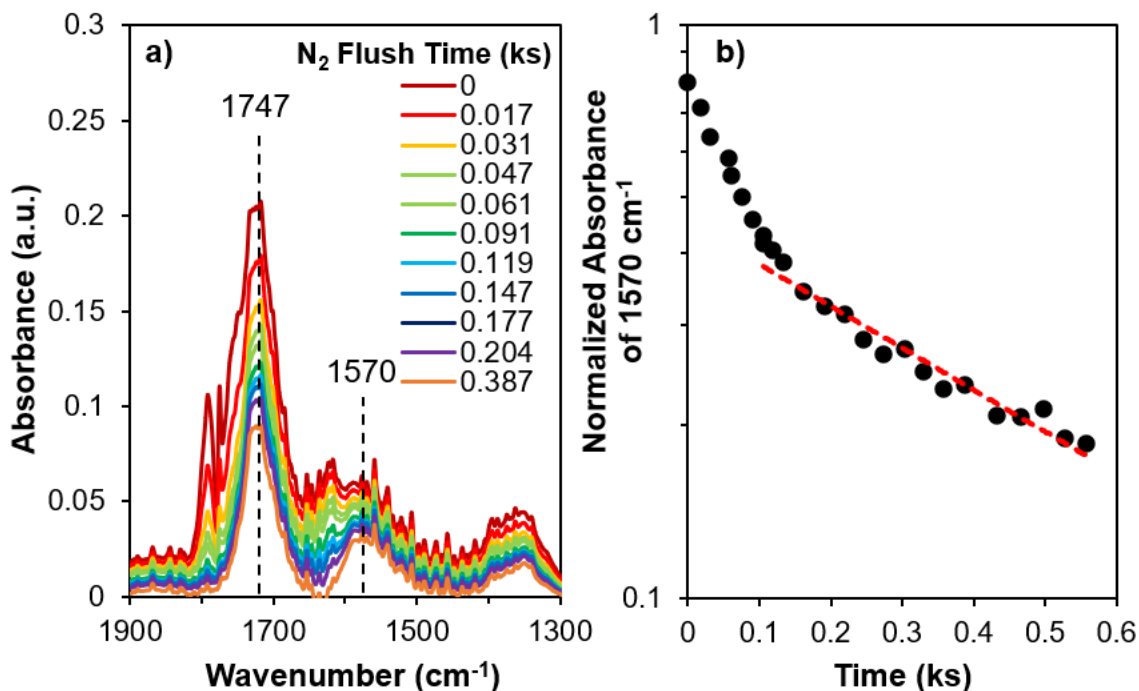


Figure 3.9. **a)** Infrared spectra of Pd/SiO₂ (1% wt.) measured during steady-state HCOOH catalysis (0.84 kPa, 353 K) and in flowing N₂ (at 353 K) after the removal of HCOOH(g) from the reactant stream. **b)** Normalized absorbance for infrared bands for HCOOH* (at 1570 cm⁻¹) on Pd/SiO₂ (1% wt.) as a function of time in flowing N₂ (at 353 K); these values are normalized by their steady-state value ($t < 0$) before flowing N₂. Dashed line represents the regression of the data to the first-order decomposition reaction.

3.4.2.3. Kinetic Isotope Effects

Kinetic isotope effects were used to analyze the kinetically relevant steps and provide insight into how HCOOH* decomposes. The kinetic isotope effects were measured on 1% wt. Pd/SiO₂ in the presence of HCOOH, DCOOH, and HCOOD (0.17-3.36 kPa, 373 K). Figure 3.10 shows that the dehydrogenation rates decrease as the O-H and C-H bonds are substituted with O-D and C-D bonds for HCOOD and DCOOH by factors 5.6 and 3.7, respectively. These results suggest that the kinetically relevant step involves the concurrent cleavage of O-H and C-H bonds. More rigorous analysis of kinetic isotope effects on rate and equilibrium constants requires fitting the data to the rate equation derived from the proposed elementary steps. These results are discussed in the next section.

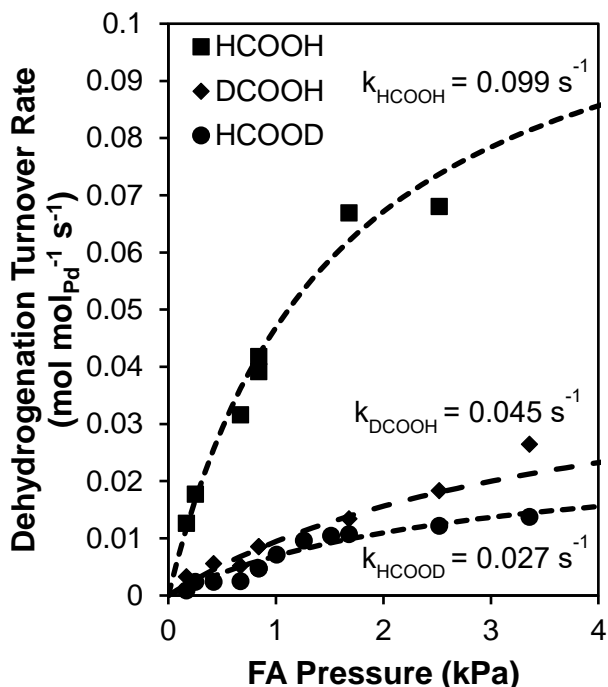
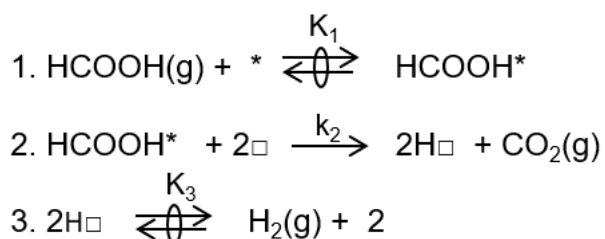


Figure 3.10. Dehydrogenation turnover rates of HCOOH, DCOOH, and HCOOD (per surface Pd atom) on Pd/SiO₂ (1% wt.) as a function of HCOOH pressure (0.17-3.36 kPa; 373 K). Dashed curves represent the optimal regression rates using the functional form of Eq. (3.1).

3.4.2.6. HCOOH Dehydrogenation Reaction Mechanism

Scheme 3.1. shows the proposed elementary steps based on the results from the kinetic, isotopic, and spectroscopic studies discussed thus far.



Scheme 3.1. Proposed sequence of elementary steps for molecular HCOOH dehydrogenation. Quasi-equilibrated steps are denoted by ovals in double arrows. Active sites denoted represent the atop site (*) and hollow site (□).

HCOOH adsorbs to the Pd surface as HCOOH*. The O-H and C-H bonds are then activated simultaneously, causing the HCOOH* to decompose into two H* and CO₂(g) (“*” and “□” indicate the atop and hollow active site respectively). Lastly, the H*

atoms recombine and desorb as H₂(g). Based on the isotopic experiments, it was assumed that steps 1 and 3 of the mechanism are quasi-equilibrated while step 2 is the rate-limiting step, as indicated by the cleaving of the C-H and O-H bond being kinetically relevant. The process of deriving the rate equation is discussed below. Using the quasi-equilibrated assumption on step 1 and step 3, we get:

$$[HCOOH^*] = K_1 P_{HCOOH} [^*] \quad (3.3)$$

$$K_3 = \frac{[H^*][H_2O]}{P_{H_2} [^*][\square]} \quad (3.4)$$

Given that HCOOH* is the reaction mechanism and the reaction is not H₂ dependent, a site balance gives:

$$[^*] + [HCOOH^*] = 1 \quad (3.5)$$

Combining Eq. (3.3) and Eq. (3.5) and solving for [*] (Eq. (3.4) is not needed because it is not an H₂-dependent reaction):

$$[^*] = \frac{1}{1 + K_1 P_{HCOOH}} \quad (3.6)$$

The HCOOH dehydrogenation rate is determined by the rate of step 2:

$$r = r_2 = k_2 [HCOOH^*][\square] \quad (3.7)$$

Due to the lack of H₂ dependency, we can neglect [□]. The overall reaction rate follows the Langmuir equation as assumed during kinetic analysis:

$$r = \frac{k_2 K_1 P_{HCOOH}}{1 + K_1 P_{HCOOH}} \quad (3.8)$$

The steady-state data for the dehydrogenation reaction was also utilized to calculate k₂ and K₁ by fitting Eq. (3.8) to the experimental data. The results of fitting these parameters to the experimental data are shown in Table (3.2). From these parameters, the additional thermodynamic components of rate and equilibrium constants were calculated utilizing Eq. (3.11) and Eq. (3.14) from the fitted k₂ and K₁ values:

$$K = \exp\left(\frac{-\Delta G}{RT}\right) \quad (3.9)$$

$$K = \exp\left(\frac{\Delta S}{R}\right) \exp\left(\frac{-\Delta H}{RT}\right) \quad (3.10)$$

$$\ln(K) = \frac{-\Delta H}{R} * \frac{1}{T} + \frac{\Delta S}{R} \quad (3.11)$$

$$k = \frac{k_B T}{h} \exp\left(\frac{-\Delta G^\ddagger}{RT}\right) \quad (3.12)$$

$$k = \frac{k_B T}{h} \exp\left(\frac{\Delta S^\ddagger}{R}\right) \exp\left(\frac{-\Delta H^\ddagger}{RT}\right) \quad (3.13)$$

$$\ln(k) = \frac{-\Delta H^\ddagger}{R} * \frac{1}{T} + \frac{\Delta S^\ddagger}{R} + \ln\left(\frac{k_B T}{h}\right) \quad (3.14)$$

The calculated Gibbs free energy of reaction (ΔG) and activation energy (ΔG^\ddagger) are provided in Table 3.3 along with the corresponding enthalpy (ΔH) and entropy values (ΔS).

The kinetic isotope effects (KIE) on the constant k were obtained by regressing the experimental rate data for the dehydrogenation of HCOOH, DCOOH, and HCOOD using the functional form of Equation 3.1. Table 3.3 summarizes the KIE result. KIE values are defined as the ratio of k for the different isotopes.

Table 3.2. Equilibrium and rate constants and the corresponding enthalpies and entropies from kinetic analysis.

	ΔS (kJ mol ⁻¹ K ⁻¹)	ΔH (kJ mol ⁻¹)	ΔG_{353K} (kJ mol ⁻¹)
K_{353K}			
136.37	-0.08	-44.19	-14.43
k_{353K} (s⁻¹)	ΔS^\ddagger (kJ mol⁻¹ K⁻¹)	ΔH^\ddagger (kJ mol⁻¹)	ΔG^\ddagger_{353K} (kJ mol⁻¹)
0.010	0.07	125.33	100.6

All kinetic data (0.17-3.36 kPa HCOOH, 353-383 K; Figure 3.2) are fitted simultaneously to the functional form of Eq. (3.1) within a packed bed reactor to obtain the respective enthalpic and entropic components. K_{353K} and k_{353K} constants are obtained by using the sum of squares method between the experimental and fitted data. The corresponding enthalpy, entropy, and Gibbs free energy were obtained by plotting the $\ln(k)$ and $\ln(K)$ with $1/\text{Temperature}$ to get the corresponding values from the slope and intersection of Eq. (3.11) and Eq. (3.14).

Table 3.3. Kinetic isotope effects on equilibrium and rate constants from experiments.

k	
HCOOH/DCOOH	2.6
HCOOH/HCOOD	4.4

Values of k were found by using sum of squares method to regress Eq. (3.1) over the experimental data for HCOOH, HCOOD, and DCOOH (0.17-3.36 kPa; 373 K; Figure 3.10).

3.4.2.5. Temperature Programmed Desorption

TPD was utilized to determine the number of HCOOH species adsorbed per Pd site on the 1% wt. Pd/SiO₂ catalyst (Figure 3.11). It was found that CO₂ desorbed from the catalyst around 350 K. No desorbed HCOOH or H₂ was observed; however, the mass spectrometer was not capable of accurately detecting the H₂. TPD conducted on SiO₂ showed no detection of HCOOH adsorbing to the surface, or HCOOH or H₂ desorbing. From the calculated area under the CO₂ peak, it was found that number of active sites per mol of Pd was 0.85. This indicates that exactly one HCOOH adsorbed to each Pd nanoparticle during HCOOH dehydrogenation.

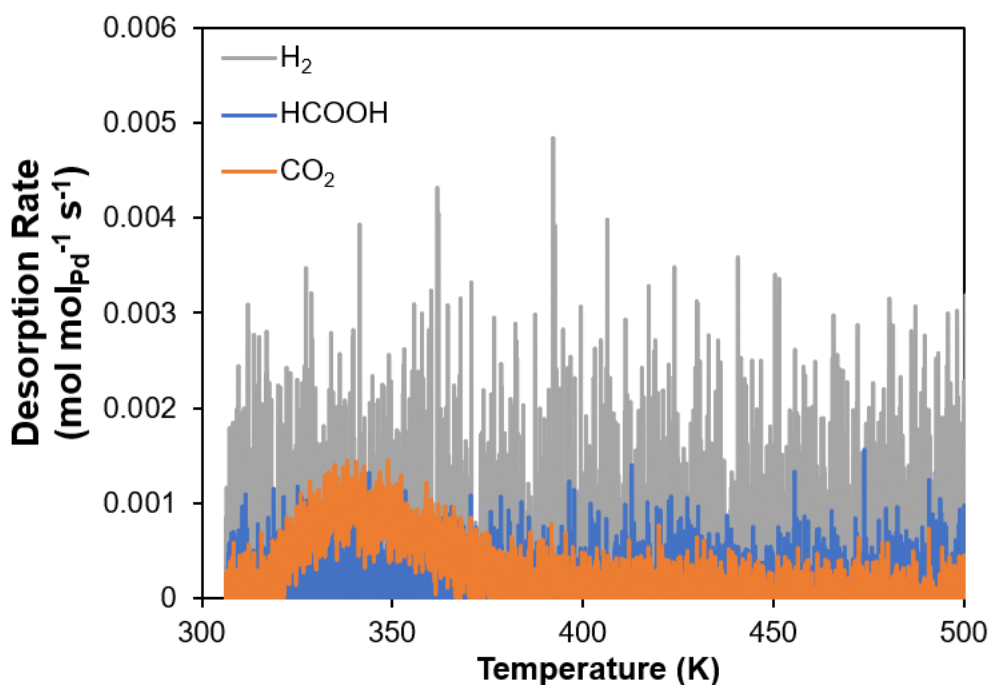


Figure 3.11. TPD of HCOOH on Pd/SiO₂ (1% wt.) showing HCOOH, CO₂ and H₂ desorption rate as a function of temperature.

3.4.3. Pd Size Effects

The particle size effects of the Pd/SiO₂ catalysts were observed by adjusting the loading (0.05%, 0.1%, and 1% wt.). The turnover rates (per Pd atom) differed drastically from a loading of 1% to 0.1% (0.1-3.5 kPa HCOOH, 363 K, Figure 3.12). This change indicates the strong effects of Pd nanoparticle size on the surface reactivity. Smaller loading was assumed to result in smaller particle sizes due to the amount of Pd added. Literature suggests a strong correlation between particle sizes and reaction rates, with larger particle sizes resulting in lower reaction rates⁵⁰.

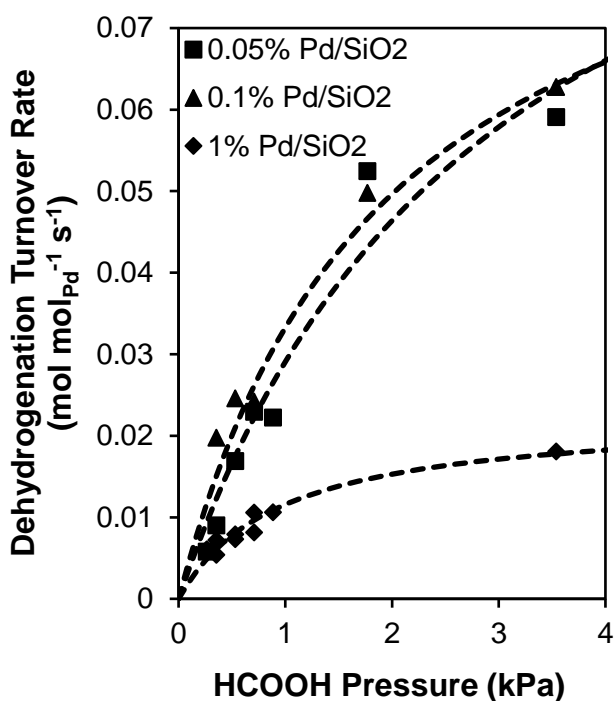


Figure 3.12. HCOOH dehydrogenation turnover rates (per Pd atom) measured on Pd/SiO₂ (0.05%, 0.1% and 1% wt.) as a function of HCOOH pressure (0.17-3.36 kPa, 363 K). Dashed curves represent the optimal regression rates using the functional form of Eq. (3.1).

Figure 3.13 compares the dehydrogenation rates over a range of HCOOH pressures (0.17-4 kPa) on Pd/SiO₂ (1% and 0.1% wt.), Pt/Al₂O₃ (2% wt.), and Au/Al₂O₃ (0.61% wt.) at 353 K. The Pt/Al₂O₃ data was obtained from a study by Ojeda et al.⁵⁸. Pt has been suggested as the most active metal for HCOOH dehydrogenation among all the transition metals²⁶. Ojeda et al., however, reported that well-dispersed Au species could achieve dehydrogenation turnover rates larger than on Pt clusters at near ambient

temperature (~350 K). Our data shows that the dehydrogenation rates increased by a factor of 1.3 for the 1% wt. Pd/SiO₂ catalyst, compared to the Pt/Al₂O₃ catalyst. These suggest that at this low temperature (353 K), Pd/SiO₂ results in dehydrogenation turnover rates of a similar magnitude compared to a Pt catalyst. The 1% wt. Pd/SiO₂ catalyst has not been shown to reach the same magnitude as the Au/Al₂O₃ catalysts. However, a smaller loading of Pd (0.1% wt.) has shown to be much closer in magnitude to the Au catalyst. This shows that the Pd/SiO₂ can achieve turnover rates greater than a Pt catalyst and close to the magnitude of well-dispersed Au at near ambient temperatures (353 K).

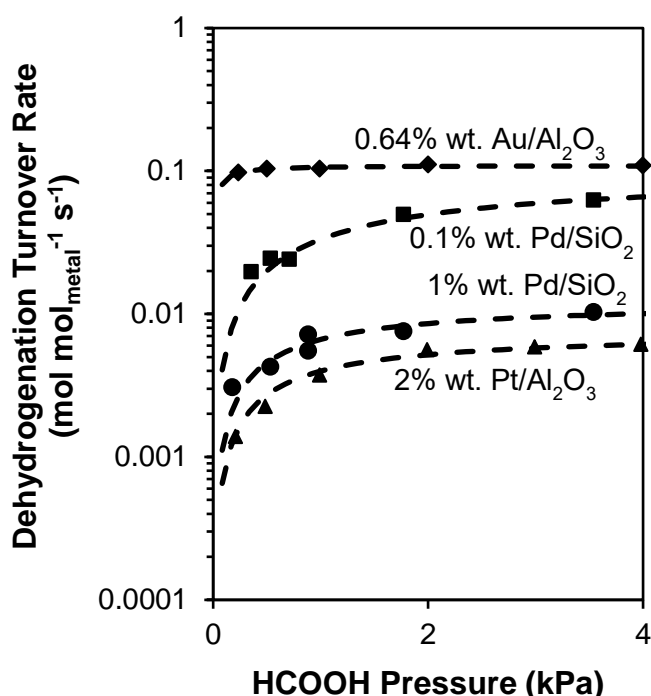


Figure 3.13. HCOOH dehydrogenation turnover rates (per surface metal) on Au/Al₂O₃ (0.61% wt.), Pd/SiO₂ (0.1% and 1% wt.) and Pt/Al₂O₃ (2% wt.) as a function of HCOOH pressure (0.17-4 kPa, 353 K). Au/Al₂O₃ and Pt/Al₂O₃ data obtained from Ojeda et al.⁵⁸. Dashed curves represent the optimal regression rates using the functional form of Eq. (3.1) for Pd/SiO₂ catalyst.

3.5. Conclusion

In this work, the dehydrogenation of HCOOH on a Pd/SiO₂ catalyst was studied. The reactivity, selectivity, and stability were analyzed to determine if this catalyst merits further consideration for industrial use. Pd/SiO₂ was found to be stable and selective towards dehydrogenation products at near ambient temperatures (353-383 K). Additional

spectroscopic, kinetic, and isotopic methods were utilized to determine that HCOOH decomposes through an HCOOH* intermediate to form CO₂ and H₂, with no detectable amounts of CO (<100 ppb). Pd/SiO₂ catalysts were even found to achieve the same magnitude of HCOOH dehydrogenation rates achieved on a Pt catalyst. Overall, these results can aid in catalyst design strategies to improve the performance of Pd-based catalysts for their potential use in the HCOOH dehydrogenation reaction for its use as a liquid H₂ carrier.

3.6. Acknowledgements

This work is supported by the startup funding from Colorado School of Mines, including the Summer Undergraduate Research Fellowship (SURF) and Mines Undergraduate Research Fellowship (MURF).

CHAPTER 4

CONCLUSIONS AND FUTURE WORK

4.1. Conclusions

With the current energy and environmental crisis the world is facing, the urgency to find a clean energy source is self-evident. Liquid H₂ has emerged as a clean alternative to the current use of fossil fuels. However, there are existing storage and transportation barriers preventing the widespread utilization of H₂. The chemical storage of H₂ as HCOOH stands out as a suitable alternative to traditional cryogenic and high-pressure storage methods. This study focused on using a Pd/SiO₂ catalyst for its potential use as an effective catalyst for the HCOOH dehydrogenation reaction.

This work utilized kinetic, isotopic, and spectroscopic methods to assess the stability, selectivity, reactivity, and mechanistic details of HCOOH dehydrogenation of a Pd/SiO₂ near ambient temperatures (353-383 K). The Pd/SiO₂ catalysts were found to be active for the dehydrogenation of HCOOH at low temperatures (≤ 383 K) with no detectable amount of CO formation (<100 ppb). The dehydrogenation rates were found to follow the Langmuir equation, with the rates reaching a plateau at higher HCOOH pressures due to an HCOOH-derived intermediate saturating the surface of the catalyst. The introduction of H₂ in the reactant stream found that the dehydrogenation rate was independent of the concentration of H₂, concluding that H* and HCOOH-derived intermediates do not compete for active sites.

A reaction mechanism for the HCOOH dehydrogenation on a Pd/SiO₂ catalyst was proposed based on the combination of in-situ infrared spectroscopy, isotope, and kinetic studies. The reaction mechanism proposed included a HCOOH*-mediated pathway. HCOOH is directly adsorbed to the surface of the Pd catalyst as HCOOH*, where both H's are simultaneously cleaved to form H₂ and CO₂. The amount of Pd loaded onto the SiO₂ support significantly affected the dehydrogenation turnover rates. The Pd/SiO₂ catalyst increased the dehydrogenation turnover rate by a factor of 3 when the loading was decreased from 1% to 0.1% wt. Additionally, at low-temperature conditions, the

Pd/SiO₂ catalyst demonstrated dehydrogenation turnover rates of the same magnitude as a Pt catalyst and at even smaller loading near the same magnitude as a highly-dispersed Au catalyst. Overall, Pd/SiO₂ has been shown to be an effective catalyst for HCOOH dehydrogenation for its potential use as a liquid H₂ carrier in parallel with H₂ fuel cells.

4.2. Future Work

Future research is required to understand the extent of particle size effects on the Pd/SiO₂ catalyst. The combination of TEM and CO chemisorption will be utilized to quantitatively determine the dispersion and particle sizes of the 0.05%, 0.1%, and 1% wt. Pd/SiO₂ catalysts. In addition, the particle sizes of a 1% wt. Pd/SiO₂ catalyst will be calculated before and after oxidative treatment to determine how the ex-situ treatment affects the average particle size. In-situ infrared spectroscopy will be used with the SiO₂ support under HCOOH flow to understand which HCOOH-derived species are adsorbing to the surface of the support. This will provide insight into whether SiO₂ is affecting the number of active sites observed in TPD experiments. In-situ infrared spectroscopy will also be used with the Pd/SiO₂ catalyst at higher temperatures (>400 K) to observe if there are any differences in the surface species observed. Lastly, for this research, future work will also extend to DFT calculations to corroborate the experimental results. This will provide further insight into how HCOOH is decomposing on the surface of the Pd catalyst.

This research focused on the dehydrogenation reaction of the hydrogenation-dehydrogenation cycle of utilizing HCOOH as a potential H₂ carrier. With an efficient catalytic system, HCOOH can be used as a method to successfully establish a carbon-neutral renewable energy source. The hydrogenation part of the cycle ($\text{CO}_2(\text{g}) + \text{H}_2(\text{g}) \rightarrow \text{HCOOH}(\text{g})$) is more thermodynamically unfavorable ($\Delta G_{298\text{K}} = +48.4 \text{ kJ mol}^{-1}$)¹², requiring the development of an effective catalytic system to allow H₂ to react with CO₂. Developing this system will close the CO₂ cycle, minimizing the CO₂ emissions contributing to overall greenhouse gas emissions.

REFERENCES

- (1) Borup, R.; Krause, T.; Brouwer, J. Hydrogen Is Essential for Industry and Transportation Decarbonization. *Electrochem Soc Interface* **2021**, *30* (4), 79–84. <https://doi.org/10.1149/2.F18214IF>.
- (2) Hassan, I. A.; Ramadan, H. S.; Saleh, M. A.; Hissel, D. Hydrogen Storage Technologies for Stationary and Mobile Applications: Review, Analysis and Perspectives. *Renewable and Sustainable Energy Reviews*. Elsevier Ltd October 1, 2021. <https://doi.org/10.1016/j.rser.2021.111311>.
- (3) Graetz, J. New Approaches to Hydrogen Storage. *Chem Soc Rev* **2008**, *38* (1), 73–82. <https://doi.org/10.1039/B718842K>.
- (4) Kawanami, H.; Himeda, Y.; Laurency, G. Formic Acid as a Hydrogen Carrier for Fuel Cells Toward a Sustainable Energy System. In *Advances in Inorganic Chemistry*; Academic Press, 2017; Vol. 70, pp 395–427. <https://doi.org/10.1016/bs.adioch.2017.04.002>.
- (5) Mao, W. L.; Mao, H. Hydrogen Storage in Molecular Compounds. *Proceedings of the National Academy of Sciences* **2004**, *101* (3), 708–710. <https://doi.org/10.1073/pnas.0307449100>.
- (6) Colón, Y. J.; Fairen-Jimenez, D.; Wilmer, C. E.; Snurr, R. Q. High-Throughput Screening of Porous Crystalline Materials for Hydrogen Storage Capacity near Room Temperature. *The Journal of Physical Chemistry C* **2014**, *118* (10), 5383–5389. <https://doi.org/10.1021/jp4122326>.
- (7) Suh, M. P.; Park, H. J.; Prasad, T. K.; Lim, D.-W. Hydrogen Storage in Metal–Organic Frameworks. *Chem Rev* **2012**, *112* (2), 782–835. <https://doi.org/10.1021/cr200274s>.
- (8) Murray, L. J.; Dincă, M.; Long, J. R. Hydrogen Storage in Metal–Organic Frameworks. *Chem Soc Rev* **2009**, *38* (5), 1294. <https://doi.org/10.1039/b802256a>.
- (9) Lim, W.-X.; Thornton, A. W.; Hill, A. J.; Cox, B. J.; Hill, J. M.; Hill, M. R. High Performance Hydrogen Storage from Be-BTB Metal–Organic Framework at Room Temperature. *Langmuir* **2013**, *29* (27), 8524–8533. <https://doi.org/10.1021/la401446s>.
- (10) Viswanathan, B. Hydrogen Storage. In *Energy Sources*; Elsevier, 2017; pp 185–212. <https://doi.org/10.1016/B978-0-444-56353-8.00010-1>.
- (11) Andersson, J.; Grönkvist, S. Large-Scale Storage of Hydrogen. *Int J Hydrogen Energy* **2019**, *44* (23), 11901–11919. <https://doi.org/10.1016/j.ijhydene.2019.03.063>.
- (12) Schlüssel, S.; Kwon, S. A Review of Formic Acid Decomposition Routes on Transition Metals for Its Potential Use as a Liquid H₂ Carrier. *Korean*

- Journal of Chemical Engineering* **2022**, 39 (11), 2883–2895.
<https://doi.org/10.1007/s11814-022-1276-z>.
- (13) *CAMEO Chemicals - PubChem Data Source*.
<https://pubchem.ncbi.nlm.nih.gov/source/11944> (accessed 2022-05-22).
- (14) Kothandaraman, J.; Kar, S.; Sen, R.; Goepfert, A.; Olah, G. A.; Prakash, G. K. S. Efficient Reversible Hydrogen Carrier System Based on Amine Reforming of Methanol. *J Am Chem Soc* **2017**, 139 (7), 2549–2552.
<https://doi.org/10.1021/jacs.6b11637>.
- (15) Aziz, M.; Oda, T.; Kashiwagi, T. Comparison of Liquid Hydrogen, Methylcyclohexane and Ammonia on Energy Efficiency and Economy. *Energy Procedia* **2019**, 158, 4086–4091.
<https://doi.org/10.1016/j.egypro.2019.01.827>.
- (16) Aziz, M.; Wijayanta, A. T.; Nandiyanto, A. B. D. Ammonia as Effective Hydrogen Storage: A Review on Production, Storage and Utilization. *Energies (Basel)* **2020**, 13 (12), 3062. <https://doi.org/10.3390/en13123062>.
- (17) *DOE Technical Targets for Onboard Hydrogen Storage for Light-Duty Vehicles | Department of Energy*. <https://www.energy.gov/eere/fuelcells/doe-technical-targets-onboard-hydrogen-storage-light-duty-vehicles> (accessed 2023-11-15).
- (18) Liu, X.; Elgowainy, A.; Wang, M. Life Cycle Energy Use and Greenhouse Gas Emissions of Ammonia Production from Renewable Resources and Industrial By-Products. *Green Chemistry* **2020**, 22 (17), 5751–5761.
<https://doi.org/10.1039/D0GC02301A>.
- (19) Torrente-Murciano, L.; Smith, C. Process Challenges of Green Ammonia Production. *Nature Synthesis* **2023**, 2 (7), 587–588.
<https://doi.org/10.1038/s44160-023-00339-x>.
- (20) Álvarez, A.; Bansode, A.; Urakawa, A.; Bavykina, A. V.; Wezendonk, T. A.; Makkee, M.; Gascon, J.; Kapteijn, F. Challenges in the Greener Production of Formates/Formic Acid, Methanol, and DME by Heterogeneously Catalyzed CO₂ Hydrogenation Processes. *Chem Rev* **2017**, 117 (14), 9804–9838.
https://doi.org/10.1021/ACS.CHEMREV.6B00816/ASSET/IMAGES/LARGE/CR-2016-00816H_0019.JPEG.
- (21) Loges, B.; Boddien, A.; Junge, H.; Beller, M. Controlled Generation of Hydrogen from Formic Acid Amine Adducts at Room Temperature and Application in H₂/O₂ Fuel Cells. *Angewandte Chemie International Edition* **2008**, 47 (21), 3962–3965. <https://doi.org/10.1002/ANIE.200705972>.
- (22) Sanchez, F.; Motta, D.; Roldan, A.; Hammond, C.; Villa, A.; Dimitratos, N. Hydrogen Generation from Additive-Free Formic Acid Decomposition Under Mild Conditions by Pd/C: Experimental and DFT Studies. *Top Catal* **2018**, 61 (3–4), 254–266. <https://doi.org/10.1007/s11244-018-0894-5>.

- (23) Navlani-García, M.; Mori, K.; Salinas-Torres, D.; Kuwahara, Y.; Yamashita, H. New Approaches toward the Hydrogen Production from Formic Acid Dehydrogenation over Pd-Based Heterogeneous Catalysts. *Frontiers in Materials*. Frontiers Media S.A. March 8, 2019. <https://doi.org/10.3389/fmats.2019.00044>.
- (24) Columbia, M. R.; Crabtree, A. M.; Thiel, P. A. Effect of CO on Pt-Catalyzed Decomposition of Formic Acid in Ultrahigh Vacuum. *Journal of Electroanalytical Chemistry* **1993**, 345 (1–2), 93–105. [https://doi.org/10.1016/0022-0728\(93\)80471-S](https://doi.org/10.1016/0022-0728(93)80471-S).
- (25) He, N.; Li, Z. H. Palladium-Atom Catalyzed Formic Acid Decomposition and the Switch of Reaction Mechanism with Temperature. *Physical Chemistry Chemical Physics* **2016**, 18 (15), 10005–10017. <https://doi.org/10.1039/C6CP00186F>.
- (26) Tang, Y.; Roberts, C. A.; Perkins, R. T.; Wachs, I. E. Revisiting Formic Acid Decomposition on Metallic Powder Catalysts: Exploding the HCOOH Decomposition Volcano Curve. *Surf Sci* **2016**, 650, 103–110. <https://doi.org/10.1016/j.susc.2015.12.032>.
- (27) Kim, Y.; Kim, S.; Ham, H. C.; Kim, D. H. Mechanistic Insights on Aqueous Formic Acid Dehydrogenation over Pd/C Catalyst for Efficient Hydrogen Production. *J Catal* **2020**, 389, 506–516. <https://doi.org/10.1016/j.jcat.2020.06.033>.
- (28) Jones, S.; Kolpin, A.; Tsang, S. C. E. Modification of Pd for Formic Acid Decomposition by Support Grafted Functional Groups. *Catalysis, Structure & Reactivity* **2014**, 1 (1), 19–24. <https://doi.org/10.1179/2055075814Y.0000000004>.
- (29) Kim, Y.; Lee, H.; Yang, S.; Lee, J.; Kim, H.; Hwang, S.; Jeon, S. W.; Kim, D. H. Ultrafine Pd Nanoparticles on Amine-Functionalized Carbon Nanotubes for Hydrogen Production from Formic Acid. *J Catal* **2021**, 404, 324–333. <https://doi.org/10.1016/j.jcat.2021.10.007>.
- (30) Hu, C.; Pulleri, J. K.; Ting, S.-W.; Chan, K.-Y. Activity of Pd/C for Hydrogen Generation in Aqueous Formic Acid Solution. *Int J Hydrogen Energy* **2014**, 39 (1), 381–390. <https://doi.org/10.1016/j.ijhydene.2013.10.067>.
- (31) Bulut, A.; Yurderi, M.; Karatas, Y.; Zahmakiran, M.; Kivrak, H.; Gulcan, M.; Kaya, M. Pd-MnO Nanoparticles Dispersed on Amine-Grafted Silica: Highly Efficient Nanocatalyst for Hydrogen Production from Additive-Free Dehydrogenation of Formic Acid under Mild Conditions. *Appl Catal B* **2015**, 164, 324–333. <https://doi.org/10.1016/j.apcatb.2014.09.041>.
- (32) Jorgensen, S. W.; Madix, R. J. Active Oxygen on Group VIII Metals: Activation of Formic Acid and Formaldehyde on Pd(100). *J Am Chem Soc* **1988**, 110 (2), 397–400. <https://doi.org/10.1021/ja00210a014>.

- (33) Davis, J. L.; Barteau, M. A. Reactions of Carboxylic Acids on the Pd(111)-(2 × 2)O Surface: Multiple Roles of Surface Oxygen Atoms. *Surf Sci* **1991**, *256* (1–2), 50–66. [https://doi.org/10.1016/0039-6028\(91\)91199-8](https://doi.org/10.1016/0039-6028(91)91199-8).
- (34) Scaranto, J.; Mavrikakis, M. Density Functional Theory Studies of HCOOH Decomposition on Pd(111). *Surf Sci* **2016**, *650*, 111–120. <https://doi.org/10.1016/j.susc.2015.11.020>.
- (35) Zhang, R.; Liu, H.; Wang, B.; Ling, L. Insights into the Preference of CO₂ Formation from HCOOH Decomposition on Pd Surface: A Theoretical Study. *Journal of Physical Chemistry C* **2012**, *116* (42), 22266–22280. https://doi.org/10.1021/JP211900Z/ASSET/IMAGES/LARGE/JP-2011-11900Z_0010.JPEG.
- (36) Li, S.; Rangarajan, S.; Scaranto, J.; Mavrikakis, M. On the Structure Sensitivity of and CO Coverage Effects on Formic Acid Decomposition on Pd Surfaces. *Surf Sci* **2021**, *709*, 121846. <https://doi.org/10.1016/j.susc.2021.121846>.
- (37) Wang, Y.; Qi, Y.; Zhang, D. New Mechanism of the Direct Pathway for Formic Acid Oxidation on Pd(111). *Comput Theor Chem* **2014**, *1049*, 51–54. <https://doi.org/10.1016/j.comptc.2014.09.020>.
- (38) Jiang, K.; Xu, K.; Zou, S.; Cai, W.-B. B-Doped Pd Catalyst: Boosting Room-Temperature Hydrogen Production from Formic Acid–Formate Solutions. *J Am Chem Soc* **2014**, *136* (13), 4861–4864. <https://doi.org/10.1021/ja5008917>.
- (39) Zhu, Q.-L.; Tsumori, N.; Xu, Q. Immobilizing Extremely Catalytically Active Palladium Nanoparticles to Carbon Nanospheres: A Weakly-Capping Growth Approach. *J Am Chem Soc* **2015**, *137* (36), 11743–11748. <https://doi.org/10.1021/jacs.5b06707>.
- (40) Song, F.-Z.; Zhu, Q.-L.; Tsumori, N.; Xu, Q. Diamine-Alkalized Reduced Graphene Oxide: Immobilization of Sub-2 Nm Palladium Nanoparticles and Optimization of Catalytic Activity for Dehydrogenation of Formic Acid. *ACS Catal* **2015**, *5* (9), 5141–5144. <https://doi.org/10.1021/acscatal.5b01411>.
- (41) Ruthven, D. M.; Upadhye, R. S. The Catalytic Decomposition of Aqueous Formic Acid over Suspended Palladium Catalysts. *J Catal* **1971**, *21* (1), 39–47. [https://doi.org/10.1016/0021-9517\(71\)90118-7](https://doi.org/10.1016/0021-9517(71)90118-7).
- (42) Li, J.; Chen, W.; Zhao, H.; Zheng, X.; Wu, L.; Pan, H.; Zhu, J.; Chen, Y.; Lu, J. Size-Dependent Catalytic Activity over Carbon-Supported Palladium Nanoparticles in Dehydrogenation of Formic Acid. *J Catal* **2017**, *352*, 371–381. <https://doi.org/10.1016/j.jcat.2017.06.007>.
- (43) Solymosi, F.; Koós, Á.; Liliom, N.; Ugrai, I. Production of CO-Free H₂ from Formic Acid. A Comparative Study of the Catalytic Behavior of Pt Metals on a Carbon Support. *J Catal* **2011**, *279* (1), 213–219. <https://doi.org/10.1016/j.jcat.2011.01.023>.

- (44) Bulushev, D. A.; Beloshapkin, S.; Ross, J. R. H. Hydrogen from Formic Acid Decomposition over Pd and Au Catalysts. *Catal Today* **2010**, *154* (1–2), 7–12. <https://doi.org/10.1016/j.cattod.2010.03.050>.
- (45) Jeroro, E.; Vohs, J. M. Reaction of Formic Acid on Zn-Modified Pd(111). *Catal Letters* **2009**, *130* (3–4), 271–277. <https://doi.org/10.1007/S10562-009-9955-5/METRICS>.
- (46) Bowker, M.; Stone, P.; Bennett, R.; Perkins, N. *Formic Acid Adsorption and Decomposition on TiO₂ (1 1 0) and on Pd/TiO₂ (1 1 0) Model Catalysts*. www.elsevier.com/locate/susc.
- (47) Rahbari, A.; Ramdin, M.; van den Broeke, L. J. P.; Vlugt, T. J. H. Combined Steam Reforming of Methane and Formic Acid To Produce Syngas with an Adjustable H₂:CO Ratio. *Ind Eng Chem Res* **2018**, *57* (31), 10663–10674. <https://doi.org/10.1021/acs.iecr.8b02443>.
- (48) Yoo, J. S.; Abild-Pedersen, F.; Nørskov, J. K.; Studt, F. Theoretical Analysis of Transition-Metal Catalysts for Formic Acid Decomposition. *ACS Catal* **2014**, *4* (4), 1226–1233. <https://doi.org/10.1021/cs400664z>.
- (49) Vermaak, L.; Neomagus, H. W. J. P.; Bessarabov, D. G. The CO Tolerance of Pt/C and Pt-Ru/C Electrocatalysts in a High-Temperature Electrochemical Cell Used for Hydrogen Separation. *Membranes (Basel)* **2021**, *11* (9), 670. <https://doi.org/10.3390/membranes11090670>.
- (50) Kim, Y.; Kim, D. H. Understanding the Effect of Pd Size on Formic Acid Dehydrogenation via Size-Controlled Pd/C Catalysts Prepared by NaBH₄ Treatment. *Appl Catal B* **2019**, *244*, 684–693. <https://doi.org/10.1016/j.apcatb.2018.12.008>.
- (51) Wilson, N. M.; Flaherty, D. W. Mechanism for the Direct Synthesis of H₂O₂ on Pd Clusters: Heterolytic Reaction Pathways at the Liquid-Solid Interface. *J Am Chem Soc* **2016**, *138* (2), 574–586. https://doi.org/10.1021/JACS.5B10669/ASSET/IMAGES/JA-2015-10669F_M027.GIF.
- (52) Shimanouchi, T. Tables of Molecular Vibrational Frequencies. Consolidated Volume II. *J Phys Chem Ref Data* **1977**, *6* (3), 993–1102. <https://doi.org/10.1063/1.555560>.
- (53) *Formic acid*. <https://webbook.nist.gov/cgi/cbook.cgi?ID=64-18-6> (accessed 2023-12-02).
- (54) Kwon, S.; Lin, T. C.; Iglesia, E. Elementary Steps and Site Requirements in Formic Acid Dehydration Reactions on Anatase and Rutile TiO₂ Surfaces. *J Catal* **2020**, *383*, 60–76. <https://doi.org/10.1016/J.JCAT.2019.12.043>.
- (55) Cabilla, G. C.; Bonivardi, A. L.; Baltanás, M. A. Infrared Study of the Adsorption of Formic Acid on Clean and Ca-Promoted Pd/SiO₂ Catalysts.

Appl Catal A Gen **2003**, 255 (2), 181–195. [https://doi.org/10.1016/S0926-860X\(03\)00546-5](https://doi.org/10.1016/S0926-860X(03)00546-5).

- (56) Herron, J. A.; Tonelli, S.; Mavrikakis, M. Atomic and Molecular Adsorption on Pd(111). *Surf Sci* **2012**, 606 (21–22), 1670–1679. <https://doi.org/10.1016/j.susc.2012.07.003>.
- (57) Lin, T. C.; De La Torre, U.; Hejazi, A.; Kwon, S.; Iglesia, E. Unimolecular and Bimolecular Formic Acid Decomposition Routes on Dispersed Cu Nanoparticles. *J Catal* **2021**, 404, 814–831. <https://doi.org/10.1016/j.jcat.2021.08.049>.
- (58) Ojeda, M.; Iglesia, E. Formic Acid Dehydrogenation on Au-Based Catalysts at Near-Ambient Temperatures. *Angewandte Chemie International Edition* **2009**, 48 (26), 4800–4803. <https://doi.org/10.1002/ANIE.200805723>.

APPENDIX A COPYRIGHT PERMISSIONS

Permission to include previously published material in this thesis is below.

- 1) Table 1.1 is reprinted from the *Korean Journal of Chemical Engineering*, Vol. 39, Sierra Schlussek et al., "A Review of Formic Acid Decomposition Routes on Transition Metals for its Potential Use as a Liquid H₂ Carrier," 2883-2895, (2022), using the following permission from the publisher, Springer Nature:

SPRINGER NATURE LICENSE TERMS AND CONDITIONS

Nov 09, 2023

This Agreement between Colorado School of Mines -- Sierra Schlussek ("You") and Springer Nature ("Springer Nature") consists of your license details and the terms and conditions provided by Springer Nature and Copyright Clearance Center.

License Number	5657781049217
License date	Oct 28, 2023
Licensed Content Publisher	Springer Nature
Licensed Content Publication	Korean Journal of Chemical Engineering
Licensed Content Title	A review of formic acid decomposition routes on transition metals for its potential use as a liquid H ₂ carrier
Licensed Content Author	Sierra Schlussek et al
Licensed Content Date	Oct 10, 2022
Type of Use	Thesis/Dissertation
Requestor type	academic/university or research institute
Format	electronic
Portion	figures/tables/illustrations
Number of figures/tables/illustrations	1
Will you be translating?	no
Circulation/distribution	1 - 29
Author of this Springer Nature content	yes
Title of new work	Mechanism of Formic Acid Decomposition on Palladium Silica Catalyst
Institution name	Colorado School of Mines
Expected presentation date	Nov 2023
Portions	Table 1
Requestor Location	Colorado School of Mines 1500 Illinois St GOLDEN, CO 80401 United States Attn: Colorado School of Mines
Total	0.00 USD

Terms and Conditions

Springer Nature Customer Service Centre GmbH Terms and Conditions

The following terms and conditions ("Terms and Conditions") together with the terms specified in your [RightsLink] constitute the License ("License") between you as Licensee and Springer Nature Customer Service Centre GmbH as Licensor. By clicking 'accept' and completing the transaction for your use of the material ("Licensed Material"), you confirm your acceptance of and obligation to be bound by these Terms and Conditions.

2) Figure 1.2 is reprinted from *Surface Science*, Vol. 650, Yadan Tang et al., “Revisiting formic acid decomposition on metallic power catalysts: Exploding the HCOOH decomposition volcano curve,” 103-110, (2016), using the following permission from the publisher, Elsevier:

ELSEVIER LICENSE TERMS AND CONDITIONS

Nov 09, 2023

This Agreement between Colorado School of Mines -- Sierra Schlussek ("You") and Elsevier ("Elsevier") consists of your license details and the terms and conditions provided by Elsevier and Copyright Clearance Center.

License Number	5657790225755
License date	Oct 28, 2023
Licensed Content Publisher	Elsevier
Licensed Content Publication	Surface Science
Licensed Content Title	Revisiting formic acid decomposition on metallic powder catalysts: Exploding the HCOOH decomposition volcano curve
Licensed Content Author	Yadan Tang, Charles A. Roberts, Ryan T. Perkins, Israel E. Wachs
Licensed Content Date	Aug 1, 2016
Licensed Content Volume	650
Licensed Content Issue	n/a
Licensed Content Pages	8
Start Page	103
End Page	110
Type of Use	reuse in a thesis/dissertation
Portion	figures/tables/illustrations
Number of figures/tables/illustrations	1
Format	electronic
Are you the author of this Elsevier article?	No
Will you be translating?	No
Title of new work	Mechanism of Formic Acid Decomposition on Palladium Silica Catalyst
Institution name	Colorado School of Mines
Expected presentation date	Nov 2023
Portions	Figure 5
Requestor Location	Colorado School of Mines 1500 Illinois St GOLDEN, CO 80401 United States Attn: Colorado School of Mines 98-0397604
Publisher Tax ID	
Total	0.00 USD
Terms and Conditions	

- 3) Figure 2.1 is reprinted from the *Korean Journal of Chemical Engineering*, Vol. 39, Sierra Schlussek et al., "A Review of Formic Acid Decomposition Routes on Transition Metals for its Potential Use as a Liquid H₂ Carrier," 2883-2895, (2022), using the following permission from the publisher, Springer Nature:

SPRINGER NATURE LICENSE TERMS AND CONDITIONS

Nov 09, 2023

This Agreement between Colorado School of Mines -- Sierra Schlussek ("You") and Springer Nature ("Springer Nature") consists of your license details and the terms and conditions provided by Springer Nature and Copyright Clearance Center.

License Number	5657790410157
License date	Oct 28, 2023
Licensed Content Publisher	Springer Nature
Licensed Content Publication	Korean Journal of Chemical Engineering
Licensed Content Title	A review of formic acid decomposition routes on transition metals for its potential use as a liquid H ₂ carrier
Licensed Content Author	Sierra Schlussek et al
Licensed Content Date	Oct 10, 2022
Type of Use	Thesis/Dissertation
Requestor type	academic/university or research institute
Format	electronic
Portion	figures/tables/illustrations
Number of figures/tables/illustrations	1
Will you be translating?	no
Circulation/distribution	1 - 29
Author of this Springer Nature content	yes
Title of new work	Mechanism of Formic Acid Decomposition on Palladium Silica Catalyst
Institution name	Colorado School of Mines
Expected presentation date	Nov 2023
Portions	Figure 1
Requestor Location	Colorado School of Mines 1500 Illinois St GOLDEN, CO 80401 United States Attn: Colorado School of Mines
Total	0.00 USD
Terms and Conditions	

Springer Nature Customer Service Centre GmbH Terms and Conditions

The following terms and conditions ("Terms and Conditions") together with the terms specified in your [RightsLink] constitute the License ("License") between you as Licensee and Springer Nature Customer Service Centre GmbH as Licensor. By clicking 'accept' and completing the transaction for your use of the material ("Licensed Material"), you confirm your acceptance of and obligation to be bound by these Terms and Conditions.

4) Figure 2.2 is reprinted from *Surface Science*, Vol. 709, Sha Li et al., "On the structure sensitivity of and CO coverage effects on formic acid decomposition on Pd surfaces," 121846, (2021), using the following permission from the publisher, Elsevier:

ELSEVIER LICENSE TERMS AND CONDITIONS

Nov 09, 2023

This Agreement between Colorado School of Mines -- Sierra Schlusel ("You") and Elsevier ("Elsevier") consists of your license details and the terms and conditions provided by Elsevier and Copyright Clearance Center.

License Number	5657790676141
License date	Oct 28, 2023
Licensed Content Publisher	Elsevier
Licensed Content Publication	Surface Science
Licensed Content Title	On the structure sensitivity of and CO coverage effects on formic acid decomposition on Pd surfaces
Licensed Content Author	Sha Li,Srinivas Rangarajan,Jessica Scaranto,Manos Mavrikakis
Licensed Content Date	Jul 1, 2021
Licensed Content Volume	709
Licensed Content Issue	n/a
Licensed Content Pages	1
Start Page	121846
End Page	0
Type of Use	reuse in a thesis/dissertation
Portion	figures/tables/illustrations
Number of figures/tables/illustrations	1
Format	electronic
Are you the author of this Elsevier article?	No
Will you be translating?	No
Title of new work	Mechanism of Formic Acid Decomposition on Palladium Silica Catalyst
Institution name	Colorado School of Mines
Expected presentation date	Nov 2023
Portions	Figure 4
Requestor Location	Colorado School of Mines 1500 Illinois St GOLDEN, CO 80401 United States Attn: Colorado School of Mines
Publisher Tax ID	98-0397604
Total	0.00 USD
Terms and Conditions	

- 5) Figure 2.3 is reprinted from *Applied Catalysis B: Environmental*, Vol. 244, Yongwoo Kim et al., “Understanding the effect of Pd size on formic acid dehydrogenation via size-controlled Pd/C catalysts prepared by NaBH₄ treatment,” 684-693, (2019), using the following permission from the publisher, Elsevier:

ELSEVIER LICENSE TERMS AND CONDITIONS

Nov 09, 2023

This Agreement between Colorado School of Mines -- Sierra Schlusel ("You") and Elsevier ("Elsevier") consists of your license details and the terms and conditions provided by Elsevier and Copyright Clearance Center.

License Number	5657791098265
License date	Oct 28, 2023
Licensed Content Publisher	Elsevier
Licensed Content Publication	Applied Catalysis B: Environmental
Licensed Content Title	Understanding the effect of Pd size on formic acid dehydrogenation via size-controlled Pd/C catalysts prepared by NaBH ₄ treatment
Licensed Content Author	Yongwoo Kim, Do Heui Kim
Licensed Content Date	5 May 2019
Licensed Content Volume	244
Licensed Content Issue	n/a
Licensed Content Pages	10
Start Page	684
End Page	693
Type of Use	reuse in a thesis/dissertation
Portion	figures/tables/illustrations
Number of figures/tables/illustrations	1
Format	electronic
Are you the author of this Elsevier article?	No
Will you be translating?	No
Title of new work	Mechanism of Formic Acid Decomposition on Palladium Silica Catalyst
Institution name	Colorado School of Mines
Expected presentation date	Nov 2023
Portions	Figure 10
Requestor Location	Colorado School of Mines 1500 Illinois St GOLDEN, CO 80401 United States Attn: Colorado School of Mines
Publisher Tax ID	98-0397604
Total	0.00 USD
Terms and Conditions	